

Rupture Models of the Great 1700 Cascadia Earthquake Based on  
Microfossil Paleoseismic Observations

by

Pei-Ling Wang

M.Sc., National Taiwan University, 2010

B.A., National Taipei University, 2007

A Thesis Submitted in Partial Fulfillment  
of the Requirements for the Degree of

MASTER OF SCIENCE

in the School of Earth and Ocean Sciences

© Pei-Ling Wang, 2012  
University of Victoria

All rights reserved. This thesis may not be reproduced in whole or in part, by photocopy  
or other means, without the permission of the author.

## **Supervisory Committee**

Rupture Models of the Great 1700 Cascadia Earthquake Based on  
Microfossil Paleoseismic Observations

by

Pei-Ling Wang  
M.Sc., National Taiwan University, 2010  
B.A., National Taipei University, 2007

### **Supervisory Committee**

Dr. Kelin Wang (School of Earth and Ocean Sciences)  
**Co-Supervisor**

Dr. George D. Spence (School of Earth and Ocean Sciences)  
**Co-Supervisor**

Dr. Stan E. Dosso (School of Earth and Ocean Sciences)  
**Departmental Member**

## Abstract

### Supervisory Committee

Dr. Kelin Wang (School of Earth and Ocean Sciences)

Co-Supervisor

Dr. George D. Spence (School of Earth and Ocean Sciences)

Co-Supervisor

Dr. Stan E. Dosso (School of Earth and Ocean Sciences)

Departmental Member

Past earthquake rupture models used to explain paleoseismic estimates of coastal subsidence during the great AD 1700 Cascadia earthquake have assumed a uniform slip distribution along the megathrust. Here, we infer heterogeneous slip for the Cascadia margin in AD 1700 that is analogous to slip distributions during instrumentally recorded great subduction earthquakes worldwide. The assumption of uniform distribution in previous rupture models was due partly to the large uncertainties of available paleoseismic data used to constrain the models. In this work, we use more precise estimates of subsidence in 1700 from detailed tidal microfossil studies. We develop a 3-D elastic dislocation model that allows the slip to vary both along strike and in the dip direction. Despite uncertainties in the updip and downdip slip extents, the more precise subsidence estimates are best explained by a model with along-strike slip heterogeneity, with multiple patches of high moment release separated by areas of low moment release. For example, in AD 1700 there was very little slip near Alsea Bay, Oregon ( $\sim 44.5^\circ\text{N}$ ), an area that coincides with a segment boundary previously suggested on the basis of gravity anomalies. A probable subducting seamount in this area may be responsible for impeding rupture during great earthquakes. Our results highlight the need for precise, high-quality estimates of subsidence or uplift during prehistoric earthquakes from the coasts of southern British Columbia, northern Washington (north of  $47^\circ\text{N}$ ), southernmost Oregon, and northern California (south of  $43^\circ\text{N}$ ), where slip distributions of prehistoric earthquakes are poorly constrained.

## Table of Contents

Supervisory Committee .....	ii
Abstract.....	iii
Table of Contents.....	iv
List of Tables .....	vi
List of Figures.....	vii
Acknowledgments .....	ix
<b>Chapter 1. Introduction.....</b>	<b>1</b>
1.1. Motivation and objectives.....	1
1.2. Great Cascadia Earthquakes and the 1700 Event.....	3
1.3. Coseismic Slip in Other Subduction Zone Earthquakes.....	7
1.4. Collaborators' Contribution and Thesis Structure.....	11
<b>Chapter 2. Paleoseismic Observations.....</b>	<b>13</b>
2.1. Brief summary of Cascadia Paleoseismic Studies.....	13
2.1.1. Offshore Turbidite Deposits.....	14
2.1.2. Tsunami Wave Heights and Tsunami Deposits.....	15
2.1.3. Trees and Plant Roots.....	15
2.1.4. Peat-mud or Peat-sand Couplets.....	16
2.1.5. Microfossils.....	19
2.2. Foraminiferal Microfossil Studies with Transfer Function (TF) .....	21
2.3. Microfossil Paleoseismic Observations Used in This Work.....	28
2.3.1. Estimates from Transfer Function Analysis of Microfossil Data.....	28
2.3.2. Estimates from Other Analyses of Microfossil Data.....	33
2.4 Discussion.....	35
2.4.1 Uncertainties in Microfossil-based Paleo-elevation Reconstruction.....	35
2.4.2 Temporal Resolution of Paleoseismic Observations.....	36
2.4.3 Incompleteness of Paleoseismic Observations.....	37
<b>Chapter 3. Previous Work in Cascadia Megathrust Rupture Simulation</b> .....	<b>39</b>
3.1. Thermal Constraints to the Seismogenic Zone .....	39
3.2. Models of Interseismic Locking.....	41
3.3. Models of Coseismic Deformation.....	45
<b>Chapter 4. Modelling Method.....</b>	<b>49</b>
4.1. Basic Assumptions.....	49

4.2. 3-D Dislocation Model.....	50
4.3. Slip Distribution.....	52
4.4. Modeling Procedure.....	55
<b>Chapter 5. Model Results.....</b>	<b>56</b>
5.1. Uniform-Slip Models.....	56
5.2. Preferred Model.....	59
5.3. “Trench”-Breaking Rupture.....	65
5.4. Trade-off between Rupture Width and Slip Magnitude.....	67
5.5. Other Scenarios of Along-strike Variations.....	72
5.6. Discussion.....	72
5.6.1. Model Predictions in the Data Gap.....	74
5.6.2. Slip Deficit and Earthquake Reoccurrence Interval.....	76
<b>Chapter 6. Conclusions and Recommendations for Future Research</b> .....	<b>78</b>
6.1. Conclusions.....	78
6.2. Recommendations for Future Research.....	79
<b>Bibliography.....</b>	<b>84</b>

## List of Tables

Table 2.1 Paleoseismic estimates used in this study.....	30
Table 4.1 Euler poles used in this study.....	50

## List of Figures

Figure 1.1. Map of Cascadia subduction zone.....	4
Figure 1.2. A simplified cross section of a subduction zone during interseismic and coseismic periods.....	7
Figure 1.3. Slip distribution of the 2004 Sumatra earthquake.....	8
Figure 1.4. Slip distribution of the 2010 Maule (Chile) earthquake.....	9
Figure 1.5. Slip distribution of the 2011 Tohoku-Oki earthquake.....	10
Figure 2.1. Sediment samples of earthquake-related deposits.....	18
Figure 2.2. Developing a transfer function and correlating contemporary assemblages to fossil assemblages.....	22
Figure 2.3. Constructing a shore-normal training set from the upland to the tidal flat...24	
Figure 2.4. Processing foraminiferal samples in the field for identification of dominant agglutinated foraminiferal species in surface and subsurface sediment.....	25
Figure 2.5. Sampling sediment sequences.....	26
Figure 2.6. Taking samples from the outcrop at the bank of Lewis and Clark River.....	27
Figure 2.7. Previous paleoseismic studies.....	29
Figure 3.1. Updip and downdip limits of seismogenic zone in Cascadia defined by various studies.....	40
Figure 3.2. Slip deficit (backslip) distribution in the locked and transition zones.....	41
Figure 3.3. Fore-arc motion model of Wells et al. [1998] and Wells and Simpson [2001].....	43
Figure 3.4. Correction of forearc rotation.....	44
Figure 3.5. Two types of downdip distribution of coseismic slip.....	48
Figure 4.1. Structures of slab surface, fault mesh, and slip patch in the model.....	52
Figure 4.2. Slip distributions with different values of broadness $b$ and skewness $q$ .....	53
Figure 4.3. Definition of the local width ( $W$ ) and maximum width ( $W_{max}$ ) of a slip patch.....	54
Figure 5.1. Models of uniform slip along-strike (in terms of equivalent time of slip-deficit accumulation).....	58
Figure 5.2. A model modified from that shown in Figure 5.1a by varying the downdip extent of the rupture limit.....	59
Figure 5.3. The preferred model and a trench-breaking rupture model for the 1700 Cascadia earthquake.....	61
Figure 5.4. Topography, surface deformation, and fault slip distribution of the preferred model.....	63
Figure 5.5. Predicted vertical motions for the preferred model, along margin-normal profiles, and the nearest paleoseismic estimates.....	65
Figure 5.6. Tests for the effects of different downdip rupture widths.....	68
Figure 5.7. Model-predicted vertical motion for the Preferred, Wide-200, and Narrow+200 yr models along the margin-normal profile.....	69
Figure 5.8. Comparison of surface uplift magnitude and distribution, for models with different downdip rupture widths and slip.....	71
Figure 5.9. Test models with different numbers of high-slip patches.....	73

Figure 5.10. Model-predicted surface deformation by the preferred, Eight-patch, Narrow+200, and Wide-200 models continuously along the coast of Cascadia margin.....75

## Acknowledgments

I would like to thank my supervisor, **Kelin Wang**, for providing me with a great opportunity to get involved in paleoseismic studies and modeling and developing codes for my numerical models. Your guidance, inspiration, continuous help, and much patience in helping me with modeling and writing make this thesis more complete and make me more mature in doing research.

I would like to thank my committee members **George Spence** and **Stan Dosso**, and my external examiner, **Lucinda Leonard**, for your encouragements, endless support and valuable comments.

Special thanks for my collaborators **Simon E. Engelhart**, **Andrea D. Hawkes**, **Benjamin P. Horton**, **Alan R. Nelson**, and **Robert C. Witter** in re-examining previous paleoseismic observations, taking me to a fieldwork and answering related questions, and editing a large portion of my thesis.

I extend my appreciation to everyone at *Pacific Geoscience Center, Geological Survey of Canada*. In particular, thank **Honn Kao**, **Susan Bilek**, **Roy Hyndman**, **Garry Rogers**, **Earl Davis** for discussions and suggestions. Thank **Jiangheng He**, **Steve Taylor**, **Michelle Gorosh**, **Robert Kung** and **Peter Neelands** for computer support. Thank **Yanzhao Wang** and **Hongyan Chang** for support and encouragement.

Thanks many other Paleo-seismologists in discussions. Thank **Brian Atwater**, **Chris Goldfinger**, and **Anne Tréhu** for new ideas and suggestions.

I would like to extend my thanks to all the friendly and helpful people at *School of Earth and Ocean Sciences, University of Victoria* and during my M.Sc. Program. Thank faculty and staff members for your help and support, especially for **Kim Juniper** for your instruction and **Kevin Telmer** for offering a TA position. Thank my friends for your endless support. Thank **Yan Hu**, **Ikuko Wada**, **Nastasja Scholz**, **Angela Schlesinger**, and **Hyun-Seung Kim** for helping me with the new life in Victoria.

Truly appreciate the never-ending support from my home country. Special thanks for **Yeeping Chia** and **Jyr-Ching Hu** from *National Taiwan University* and **Ling Chen** and **Shenchon Lai** from *National Taipei University*.

This thesis is dedicated to my family for their endless support and encouragement.

# Chapter 1. Introduction

## 1.1. Motivation and objectives

Although there have been no instrumentally recorded great megathrust earthquakes in southwestern Canada and northwestern United States along the Cascadia subduction zone, historical records and paleoseismic evidence strongly indicate that this region is under significant risk of great earthquakes and tsunamis. Ground shaking caused by future great earthquakes may result in widespread damage along the Cascadia margin, and coastal areas are at the risk of tsunami inundation.

To understand earthquake and tsunami hazards along the Cascadia subduction zone, numerous studies have searched for evidence for prehistoric megathrust earthquakes. These studies help constrain the recurrence behavior of Cascadia megathrust earthquakes and coseismic surface elevation changes in individual events, primarily coastal subsidence. The amount and spatial extent of the elevation changes provide a measure of earthquake size, which helps to estimate the intensity and duration of shaking and the size of tsunami waves.

The most recent great Cascadia earthquake occurred in AD 1700, and the coseismic elevation changes in this event have been estimated and modeled in numerous studies. To date, rupture models for this earthquake have assumed a uniform rupture (of smoothly varying width) along the margin [e.g., *Flück et al.*, 1997; *Satake et al.*, 2003; *Leonard et al.*, 2004, 2010]. But such a uniform pattern is in sharp contrast with the heterogeneous rupture patterns of any instrumentally recorded megathrust earthquakes at other subduction zones, examples of which will be shown in Section 1.3. Because

heterogeneous slip characterizes subduction-zone earthquakes, slip during great Cascadia earthquakes must also be heterogeneous. To improve our knowledge of Cascadia earthquakes and assessment of their impact, we need to develop models that use a more realistic rupture scenarios.

Most paleoseismic observations of coseismic coastal subsidence at Cascadia have large uncertainties and thus do not help distinguish between models of uniform and variable along-strike slip distribution. The present study takes advantage of relatively new paleoseismic microfossil studies assisted by an advanced method of analysis, called the transfer functions (TF) method, to provide a more precise characterization of the earthquake rupture of 1700. Fossil assemblages of foraminifera, single-celled intertidal organisms, are correlated to modern assemblages by means of the TF. Foraminifera are sensitive to their living environment. A change in relative sea level resulting from coseismic coastal subsidence causes a recognizable change in the foraminiferal assemblages. Coseismic elevation changes estimated from TF-assisted microfossil studies thus provide much better constraints on rupture models. Different from previous uniform slip models, the new models developed in this thesis feature along-strike heterogeneity. The new models not only better explain the better-quality paleoseismic observations, but are also physically more reasonable. The newly proposed rupture models also help identify critical knowledge and data gaps in Cascadia paleoseismic studies. The improved understanding of Cascadia megathrust rupture will provide constraints for future seismic hazard assessment along the margin and contribute to the development of more realistic tsunami models for tsunami hazard assessment.

## 1.2. Great Cascadia Earthquakes and the 1700 Event

At the Cascadia subduction zone, the Juan de Fuca plate subducts obliquely beneath the North America plate (Figure 1.1). The convergence rate is roughly 35 mm/year, and ranges from ~30 mm/yr near Cape Mendocino to ~40 mm/yr near the Strait of Juan de Fuca [e.g., *Wilson*, 1993]. There is no record of large subduction earthquakes over ~200-year written history since the arrival of the first European explorers.

Before intense paleoseismic studies were carried out along the Cascadia margin, there were several explanations for the absence of great earthquakes. For example, the Juan de Fuca plate was considered to have recently stopped moving toward North America. The hypothesis was inconsistent with active volcanoes and highly deformed sediments at the base of the continental slope [*Hyndman*, 1995]. Another hypothesis was that the downgoing plate exhibits stable sliding rather than “stick-slip” behavior and hence does not generate earthquakes. An opposite hypothesis was that the plate interface is fully locked, so that there is no slip motion to generate even small earthquakes. In this case, the plate convergence builds up strain toward future earthquakes.

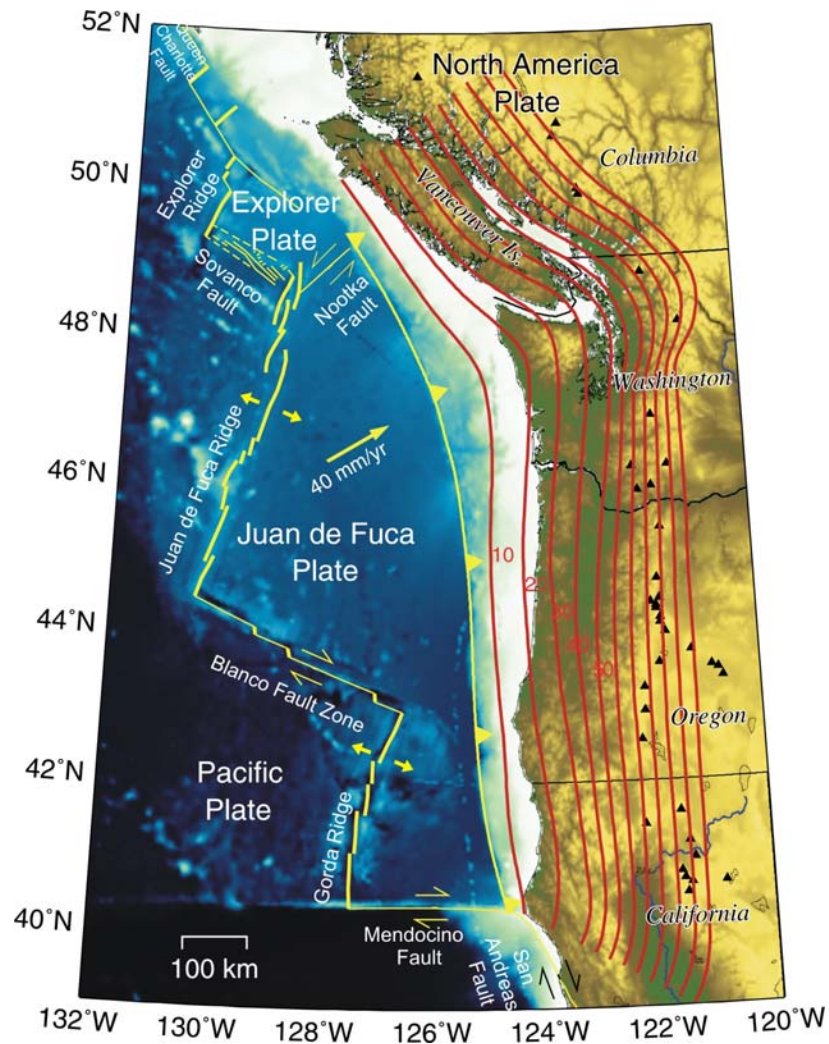


**Figure 1.1.** Map of Cascadia subduction zone. Red lines are depth contours of the subduction interface from *McCroory et al.* [2004]. Numbers are the slab depth (in km) below sea level. Black triangles denote volcanoes.

Coastal paleoseismic evidence for Cascadia megathrust earthquakes chiefly includes stratigraphic sequences of organic-rich deposits in coastal wetlands buried by tidal mud and sand [e.g., *Atwater*, 1987; *Darienzo and Peterson*, 1990; *Clague and Bobrowsky*, 1994; *Nelson et al.*, 1996a; *Atwater and Hemphill-Haley*, 1997; *Witter et al.*, 2003], with matching sudden changes in vascular plant fossils and microfossil assemblages that

suggest sudden subsidence [e.g., *Atwater and Yamaguchi*, 1991; *Guilbault et al.*, 1995; *Nelson et al.*, 1996b; *Hemphill-Haley*, 1996; *Shennan et al.*, 1996; *Kelsey et al.*, 2002; *Hughes et al.*, 2002], sometimes accompanied by tsunami-laid sand [e.g., *Darienzo and Peterson*, 1990, 1995; *Atwater*, 1992; *Darienzo et al.*, 1994; *Clague et al.*, 2000; *Witter et al.*, 2001; *Nelson et al.*, 2004; *Kelsey et al.*, 2005], or liquefaction caused by strong shaking [*Takada and Atwater*, 2004]. Along much of the Cascadia margin, offshore turbidite deposits provide the longest (10 ka) and most complete record of great megathrust earthquakes [e.g., *Goldfinger et al.*, 2012; *Atwater and Griggs*, 2012].

These studies provide strong evidence for repeated, great megathrust earthquakes over the past 3000-7000 years. The most recent event, the ~M 9 earthquake on 26 January AD 1700, is inferred from stratigraphic evidence and tsunami deposits along much of the west coast of North America, and from historical records of tsunami waves that propagated across the Pacific Ocean and caused damage in Japan [*Nelson et al.*, 1995; *Satake et al.*, 1996; *Atwater and Hemphill-Haley*, 1997; *Atwater et al.*, 2005; *Satake et al.*, 2003]. Radiocarbon dating of plant fossils in coastal stratigraphic sequences shows that the recurrence of great Cascadia earthquakes varies from less than a century to as much as 1000 years, with an average of about 300-600 years [*Atwater et al.*, 2004; *Kelsey et al.*, 2005; *Nelson et al.*, 2006]. Averages based on the frequency of offshore turbidite deposits on the continental slope and abyssal plain, assumed to have been caused by great-earthquake shaking, are lower in southern Cascadia (about 240 years) [*Goldfinger et al.*, 2012].

Evidence for coseismic coastal subsidence due to the 1700 great earthquake could be explained by the elastic deformation of the upper plate. When the subduction interface is locked, the seaward edge of the upper plate is dragged down by the downgoing oceanic plate and experiences interseismic subsidence. On the other hand, the coast, which is usually above or landward of the down-dip limit of the locked zone, is subject to upward deformation due to crustal shortening (Figure 1.2). When the accumulated stress exceeds the frictional resistance of the fault, abrupt slip occurs to cause an earthquake, and the sense of deformation is reversed. The rupture releases stored elastic strain energy and radiates outward seismic waves. The sudden uplift of the seafloor above the rupture zone is the major source of tsunami generation. After the coseismic slip, post-seismic slip of the fault and viscous stress relaxation in the mantle take place, and the fault is relocked [e.g., *Wang et al.*, 2012].

The elastic strain buildup at Cascadia is observed by Global Positioning System (GPS) [e.g., *Lisowski et al.*, 1989; *Dragert and Hyndman*, 1995] and other geodetic techniques such as repeat levelling surveys [e.g., *Reilinger and Adams*, 1982], repeated positional surveys [e.g., *Savage et al.*, 1991; *Dragert et al.*, 1994], tide gauge records [e.g., *Reilinger and Adams*, 1982; *Holdahl et al.*, 1989], and repeated gravity surveys [e.g., *Dragert et al.*, 1994]. These geodetic measurements have shown that much of the shallow part of the megathrust, located mostly offshore, is locked, and elastic strain energy is accumulating for a future rupture.

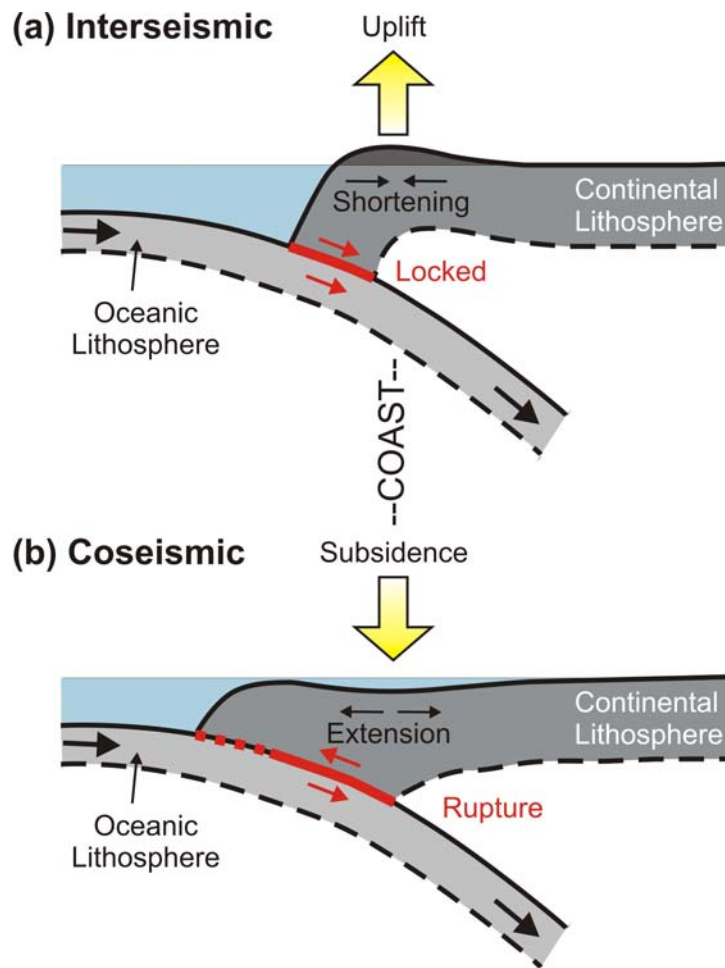


**Figure 1.2.** A simplified cross section of a subduction zone during interseismic and coseismic periods (modified from *Hyndman and Wang* [1993]). (a) During the interseismic period, the plate interface is locked. The coastal areas are uplifting gradually due to shortening in the upper plate. (b) During the coseismic period, the plate interface is unlocked. The coastal areas subside abruptly due to the extension of the upper plate.

### 1.3. Coseismic Slip in Other Subduction Zone Earthquakes

As mentioned in Section 1.1, along-strike variation in coseismic slip distribution is a primary feature of megathrust earthquakes and gives rise to the concept of asperities, that

is, patches of greater slip separated by areas of lesser slip. The most recent examples include the 2004 M 9.2 Sumatra [*Chlieh et al.*, 2007], 2010 M 8.8 Maule (Chile) [*Lorito et al.*, 2011], and 2011 M 9.0 Tohoku-Oki [e.g., *Yoshida et al.*, 2011; *Ide et al.*, 2011; *Fujii et al.*, 2011] earthquakes.

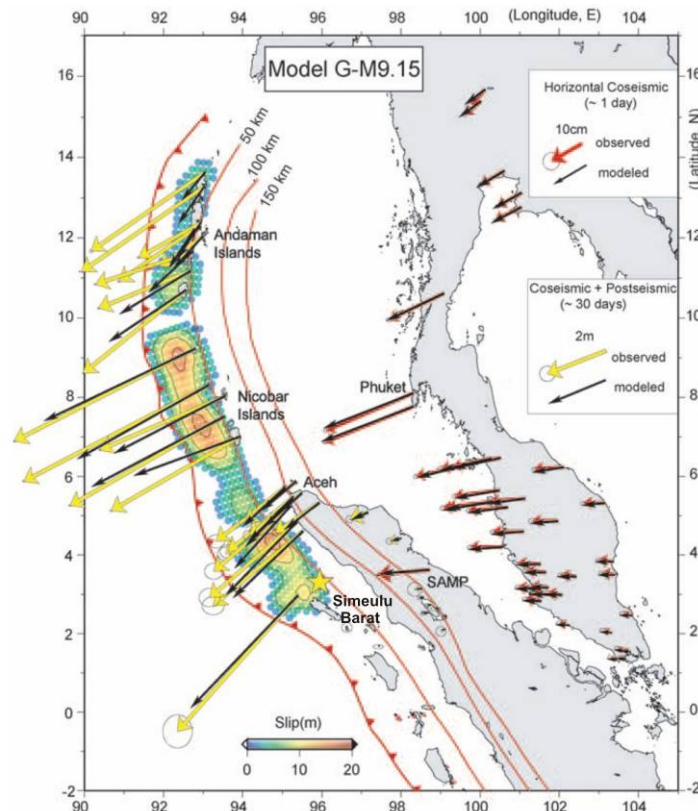


**Figure 1.3.** Slip distribution of the 2004 Sumatra earthquake (modified from *Chlieh et al.* [2007]).

The M 9.2 Sumatra earthquake of 26 December 2004 ruptured a 1500-km long segment of the Sumatra subduction zone (Figure 1.3). The rupture initiated at the megathrust below Simeulu Barat and propagated to the north (Figure 1.3). Through combined inversion of seismic and geodetic data, *Chlieh et al.* [2007] showed that the

slip distribution of the earthquake has three peaks at about 4°N, 7°N, and 9°N (Figure 1.3). Other studies also showed large variations of coseismic slip in the strike direction [e.g., *Ammon et al.*, 2005; *Subarya et al.*, 2006].

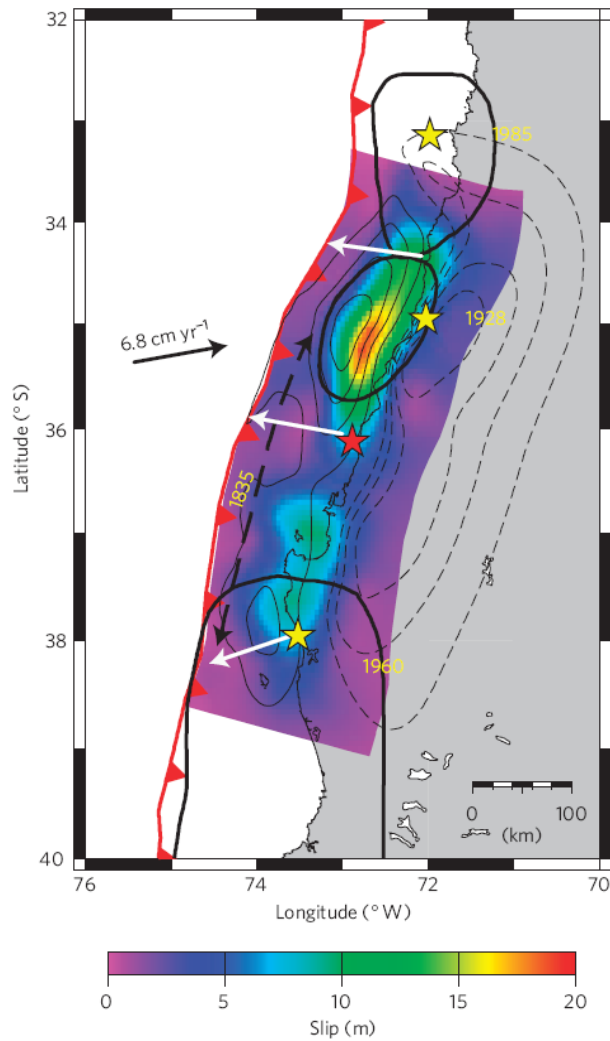


**Figure 1.4.** Slip distribution of the 2010 Maule (Chile) earthquake (from *Lorito et al.* [2011]). Black solid and dashed lines represent coseismic surface uplift and subsidence, respectively. Red star is the epicenter of the 2010 Maule earthquake. Yellow stars are epicenters of previous earthquakes with approximate source zones indicated by thick solid lines.

During the M 8.8 Maule (Chile) earthquake of 27 February 2010, the rupture broke a more than 400-km long segment of the margin. The rupture zone is north of the rupture zone of the 1960 earthquake, the largest earthquake (M 9.5) ever recorded on Earth, and in the seismic gap that had been accumulating strain since a previous M 8 event in 1835. The rupture pattern of this earthquake has been constrained by GPS observations [e.g., *Vigny et al.*, 2011], seismological data [e.g., *Farias et al.*, 2010], InSAR data [*Delouis et al.*, 2010], and tsunami observations [*Lorito et al.*, 2011]. The slip pattern determined by *Lorito et al.* [2011] through joint inversion of tsunami and geodetic data is shown in Figure 1.4.

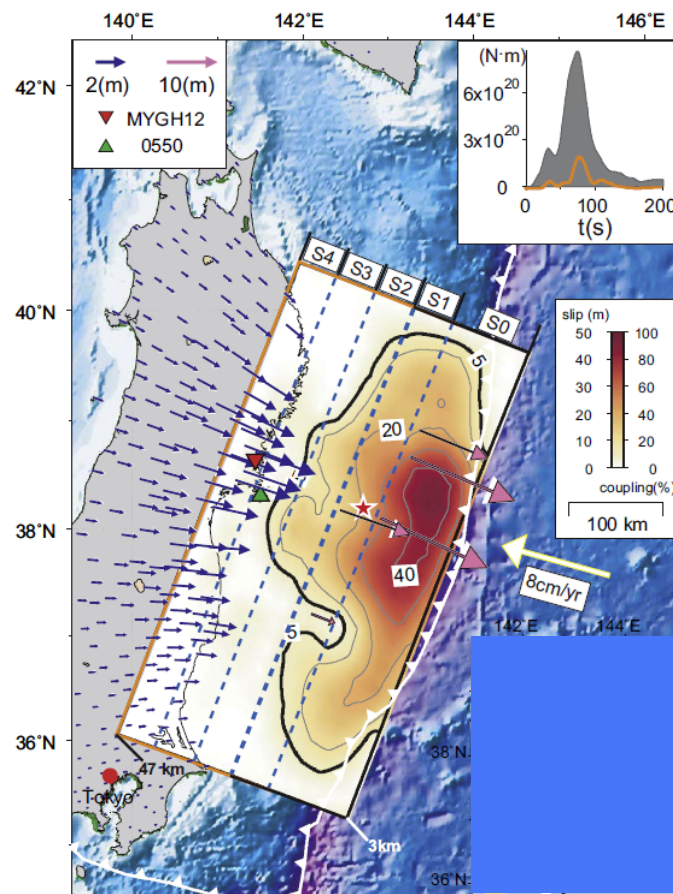


**Figure 1.5.** Slip distribution of the 2011 Tohoku-Oki earthquake (modified from *Wei et al.* [2012]). The upper right inset exhibits the moment rate function.

Heterogeneous slip is also seen in the Tohoku-Oki, Japan, earthquake of 11 March 2011 (Figure 1.5). Using tsunami waveforms, ground shaking measurements, and on-land and off-shore GPS observations, *Wei et al.* [2012] determined that the slip peaked east of the epicenter and decreased northward and southward (Figure 1.5). Other studies on tsunami waveforms [e.g., *Fujii et al.*, 2011] and seismic records [e.g., *Ide et al.*, 2011; *Yoshida et al.*, 2011] presented similar rupture patterns. Although there is only one patch, slip distribution on the plate interface is heterogeneous.

Based on the slip distribution observed in large subduction earthquakes, we know no large earthquakes that exhibit a slip distribution that is anywhere near uniform. Thus, the Cascadia subduction zone should also have exhibited heterogeneous slip during the 1700 giant earthquake.

#### **1.4. Collaborators' Contribution and Thesis Structure**

In this work, I test the hypothesis of heterogeneous, variable-slip rupture at Cascadia against new, microfossil-based estimates of coastal subsidence during the 1700 earthquake. This work is the main component of a collaborative project between the University of Victoria, Geological Survey of Canada, University of Pennsylvania, and a number of other U.S. research organizations. My collaborators Simon E. Engelhart, Andrea D. Hawkes, Benjamin P. Horton, Alan R. Nelson, Robert C. Witter, as well as my supervisor Kelin Wang, all have made substantial contributions to this research. They re-examined previous paleoseismic observations, including estimates with and without TF. Some of the estimates with TF were updated by Andrea D. Hawkes and Simon E.

Engelhart using new local TF. Simon E. Engelhart, Alan R. Nelson, Robert C. Witter, and I took additional core samples on the Oregon coast during a field trip in April 2012. In parallel with the writing of this thesis, a manuscript has been written and will be submitted to the Journal of Geophysical Research. The text of the manuscript, and hence the thesis, has been substantially edited by all the collaborators listed above.

Following the Introduction, **Chapter 2** provides a review of paleoseismic observations along the Cascadia margin and describes the newly available data used in this study. **Chapter 3** summarizes previous models in megathrust rupture simulation, both in interseismic and coseismic deformation. **Chapter 4** explains model construction and modeling procedure in this study. **Chapter 5** presents and discusses model results. In **Chapter 6**, I summarize major conclusions of this thesis and provide recommendations for future paleoseismic studies and modeling.

## Chapter 2. Paleoseismic Observations

Evidence for repeated occurrence of great earthquakes in the Cascadia subduction zone has been found in many paleoseismic studies [*Clague, 1995; Atwater et al., 1995; Leonard et al., 2004, 2010*]. Some of the paleoseismic observations provide estimates of vertical motion of the ground surface that are sufficiently accurate to constrain rupture models for these earthquakes, especially the most recent event in 1700. To explain the observations used in this thesis, this chapter provides a brief summary of various Cascadia paleoseismic studies carried out over the past more than 20 years. Among these studies, I focus on explaining a microfossil method that employs a transfer function (TF), a dataset of elevations of different contemporary foraminiferal species that can be used to correlate fossil species to paleo-elevations. Most of the estimates of coseismic elevation changes used to constrain models in this study are based on TF-assisted microfossil studies. In addition to these estimates, a few other microfossil-based estimates without the TF are also adopted.

### 2.1. Brief summary of Cascadia Paleoseismic Studies

Paleoseismic evidence for past Cascadia earthquakes includes offshore turbidite deposits, tsunami deposits, dead or injured trees and plant roots, peat-mud or peat-sand couplets, and microfossils such as diatoms and foraminifera. The study of offshore turbidite deposits, tsunami deposits, and trees and plant roots cannot yield the size of the coseismic elevation change, but they help constrain approximate time, recurrence, and rupture extents of prehistoric earthquakes. The study of peat-mud or peat-sand couplets

and microfossils gives estimates of coseismic surface deformation. In these methods, the paleo-elevation change is estimated by comparing paleo-elevation indicators in coastal sediments with modern indicators.

### **2.1.1. Offshore Turbidite Deposits**

Turbidites are sediment deposits consisting of alternating fine-grained mud layers and sandier layers on the continental slope that may form during submarine landslides triggered by seismic shaking. *Goldfinger et al.* [2008, 2012] applied Carbon-14 dating at subsea channel confluences to correlate turbidite deposits that were triggered by a common event. Based on the wide-spread turbidite distribution along the Cascadia margin, *Goldfinger et al.* [2003, 2009] proposed that the last turbidite event was triggered by the great earthquake that ruptured nearly the full length of the margin in 1700. They also suggested that the recurrence of post-Mazama-ash turbidites distributed in widely spaced submarine canyons represents earlier earthquakes similar to the 1700 event. The characteristic great earthquakes in Cascadia inferred from turbidite deposits have a recurrence interval of about 300 to 900 years. In addition to the great megathrust events, evidence for additional smaller events was found in the southernmost part of the Cascadia margin [*Goldfinger et al.*, 2003]. There is little evidence from these studies to indicate additional events in the northern region off the coast of Washington and Vancouver Island, and from the Explorer plate segment north of the Nootka fault [*Nelson et al.*, 2006; *Goldfinger et al.*, 2003, 2009] (Figure 1.1). But with very little data available for northern Cascadia, the possibility of additional events cannot be excluded [*Atwater and Griggs*, 2012].

### 2.1.2. Tsunami Wave Heights and Tsunami Deposits

Tsunami wave heights and tsunami deposits can be used to deduce the size and rupture area of an earthquake but cannot be directly used to estimate coseismic elevation changes. The height of the waves may be found in historical documents or inferred from the spatial distribution of tsunami deposits. By modeling the heights of the tsunami waves that propagated across the Pacific Ocean to reach coastal Japan in January 1700, *Satake et al.* [1996, 2003] concluded that the tsunami was generated by an earthquake of moment magnitude ( $M_w$ ) of 8.7-9.2 that ruptured the entire length of the Cascadia subduction zone. Locally along the Cascadia coast, a large tsunami would carry sand, gravel and flotsam inland and deposit them on low flat terrains. These deposits can often be seen in tidal marshes along the Cascadia coast in areas inside the subsided regions with peat-mud couplets (to be discussed in Section 2.1.3) [e.g., *Atwater, 1992; Darienzo and Peterson, 1990, 1995; Darienzo et al., 1994; Witter et al., 2001; Kelsey et al., 2005*], in areas outside the subsided regions with peat or mud sequences [*Benson et al., 1997*], and in low-lying lakes [e.g., *Clague et al., 1998, 1999*]. The coseismic deformation can be inferred indirectly from the wave heights through numerical model simulations [e.g., *Ng et al., 1991; Whitmore, 1993*].

### 2.1.3. Trees and Plant Roots

Along the Cascadia margin, trees would die when the land submerged below sea level due to coseismic surface deformation, but their roots and trunks would remain long afterward and can be used to study ancient earthquakes [*Atwater and Yamaguchi, 1991*;

*Yamaguchi et al.*, 1997; *Jacoby et al.*, 1997]. Radiocarbon ages of the stump and the growth rings of the tree block are used to constrain the time of the tree's death [*Nelson et al.*, 1995]. Based on precise radiocarbon dating and tree-ring records, *Atwater et al.* [2005] and *Nelson et al.* [2006] suggested a rupture length of > 900 km for the 1700 Cascadia earthquake. To avoid errors caused by weathering that removes the outermost rings of the trees, other studies focus on the root of the trees [*Yamaguchi et al.*, 1997], or damaged (but not killed) trees [*Jacoby et al.*, 1997]. *Atwater and Hemphill-Haley* [1997] studied plant roots that began to grow after the earthquake. Generally, paleoseismic studies based on trees and plant roots have an age uncertainty of 20-380 years or even larger [*Nelson et al.*, 1996a; *Atwater et al.*, 2004].

#### **2.1.4. Peat-mud or Peat-sand Couplets**

The formation of peat-mud or sometimes peat-sand couplets is usually attributed to coseismic subsidence. A layer of peat represents the pre-earthquake marsh surface. A layer of peat covered by a layer of muddy intertidal sediment or sometimes with a layer of sandy tsunami deposit between peat and mud indicates a sudden subsidence of coastal lowlands due to coseismic deformation [e.g., *Atwater*, 1987; *Clague and Bobrowsky*, 1994]. Two examples are shown in Figure 2.1. In both cases, the buried peat is similar to the modern peat (uppermost dark layer in Figure 2b), but is more decomposed, more compact, and lighter in color. Because organic contents of estuarine sediment increase with elevation in the intertidal zone [e.g., *Peterson and Darienzo*, 1991], interseismic uplift and sediment deposition raise the marsh surface to a higher intertidal zone and facilitate the development of organic-rich soil. The organic layer is covered by sand and mud again during the next coseismic subsidence. A peat layer overlain by mud and

grading upward into another peat layer thus can be interpreted as an earthquake cycle [Atwater, 1987].

Peat-mud or peat-sand couplets have been found at many sites along the Cascadia coast and used to reconstruct paleoelevation changes. The majority of the sites are located in southwest Washington and northwest Oregon [e.g., Atwater *et al.*, 1995; Clague, 1997; Clague *et al.*, 1998]. Because each plant species lives in a specific elevation range in the intertidal zone, paleoelevation is represented by the indicator species in the peat layer. The elevation difference, inferred from sediments that represent the marsh surfaces before and after an earthquake, represents the amounts of surface subsidence during the earthquake. The resolution of reconstructing paleoelevation based on diagnostic plants is determined by the width of the elevation range of the indicator species seen in the modern marsh; the smaller range the species is distributed over, the higher resolution is the paleoelevation estimate.

Studies of peat-mud or peat-sand couplets are based on two assumptions. First, the overlying sand or mud layers were deposited immediately after the earthquake, prior to large postseismic deformation. Second, the sediment deposits are free from the effects of compaction and other disturbances. Based on the repeated peat-mud couplets, Nelson *et al.* [2008] estimated amounts of coseismic subsidence or uplift during ancient Cascadia earthquakes. Estimates based on changes in sediment type generally range between 0.5 and 2 m, but the uncertainties are greater than 0.5 m [e.g., Atwater, 1987; Nelson *et al.*, 1996b, Atwater and Hemphill-Haley, 1997; Peterson *et al.*, 2000]. The errors in estimating coseismic subsidence based on peaty soils in buried sediment are due mainly to the large width of intertidal zones and different local conditions for peat development

at different sites [Nelson *et al.*, 1996a].



**Figure 2.1.** Sediment samples of earthquake-related deposits. White arrows indicate the sharp contact, a stratigraphic discontinuity, between peat and intertidal mud layers, representing a sudden subsidence due to the most recent great Cascadia earthquake in 1700. A tsunami might have deposited sand sheets within minutes to hours following a great earthquake, and the overlying mud might have begun accumulating within hours to days after the earthquake. (a) A Russian core, taken by a Russian core sampler (see Figure 2.5), sampled in Alsea Bay, Oregon. The peat layer is sharply overlain by medium gray tsunami-deposited sand (with arrow). (b) An excavated cutbank section at Lewis and Clark River, Oregon. The uppermost peat-sand contact (white arrow) shows the peat layer is overlain by a tsunami sand layer, an intertidal mud layer, and further up by peaty soil of the modern marsh. The repeated buried peat-mud couplets in marsh sediments

were formed during earthquake cycles (photos taken by Pei-Ling Wang during the field work in coastal Oregon in April 2012).

### **2.1.5. Microfossils**

The qualitative and semi-qualitative analyses reviewed above generally suffer from large uncertainties. Studies based on changes in lithology or organic content as discussed in Section 2.1.4 are qualitative in that they are inferred to record sudden changes from one tidal environment to another (e.g., high marsh to tide flat). With the help of measurements of the elevation ranges of modern tidal environments, semi-quantitative estimates of paleo-subsidence can be derived by comparing the elevational ranges (typically 0.5-1.0 m) for analogous paleoenvironments (inferred from lithology, fossils, or both) from above and below stratigraphic contacts thought to mark subsidence during great earthquakes. Species assemblages of statistically significant numbers of tidal microfossils (tens to hundreds in each sample), chiefly foraminifers and diatoms, give more reliable estimates of sudden paleo-environmental change than do individual plant fossils or lithology. However, as long as subsidence estimates are based on the change from one paleoenvironment to another, each with >0.5-m elevational ranges, errors on subsidence estimates remain >0.5 m and commonly >1 m [e.g., *Nelson and Kashima*, 1993; *Hemphill-Haley*, 1995; *Nelson et al.*, 1996a; *Atwater and Hemphill-Haley*, 1997; *Kelsey et al.*, 2002; *Witter et al.*, 2003; *Hawkes et al.*, 2005; *Leonard et al.*, 2010]. Because the elevational ranges of tidal environments vary from site to site, errors in these semi-quantitative subsidence estimates are difficult to assess [*Nelson et al.*, 1996a].

Present studies in reconstruction of paleoseismic surface deformation are focused mainly on microfossils, such as pollen, diatoms, or foraminifera [e.g., *Nelson and*

*Kashima*, 1993; *Hemphill-Haley*, 1995, 1996; *Nelson et al.*, 1996b; *Shennan et al.*, 1996; *Hawkes et al.*, 2010]. Coseismic subsidence can be estimated from a sudden decrease in paleoelevation (i.e., abrupt sea level rise) that is inferred from microfossils just above and below the peat-sand or peat-mud contacts. Carbon-14 dating of the fossils provides the time when the marshes were suddenly submerged and covered by sand or mud. Several methods have been applied to the analyses of tidal microfossil samples for reconstructing coseismic subsidence in Cascadia [e.g., *Hemphill-Haley*, 1995; *Nelson et al.*, 1996b, 2008; *Patterson et al.*, 2005]. Among these studies, transfer function (TF) analysis, which statistically correlates fossil assemblages to modern assemblages, is the most objective and precise [e.g., *Guilbault et al.*, 1995, 1996; *Sabean*, 2004].

Beginning in the mid-1990s, *Guilbault et al.* [1995, 1996] and *Shennan et al.* [1996; 1998] pioneered the use of statistically based microfossil analysis in estimating coseismic subsidence across contacts in Cascadia tidal sequences. *Shennan et al.*'s [1996; 1998] detrended correspondence analysis to quantitatively compare fossil assemblages of pollen and diatoms with modern assemblages of known elevation took full account of analysis errors. However, final subsidence estimates still relied on calculating a range of differences between the elevation ranges of pre-earthquake and post-earthquake paleoenvironments. *Guilbault et al.*'s [1995; 1996] approach, widely applied to microfossil assemblages from deep marine cores to reconstruct climate change, was fully quantitative in that subsidence estimates were calculated directly from fossil foraminiferal data using a TF calibrated with modern assemblage and elevation data from the same site. Their TF calculations yield subsidence estimates that have substantially smaller errors than previous methods (<0.3 m). Details in developing and applying TF in

paleoelevation estimation, in particular by studying foraminifera, will be explained in the following section.

## **2.2. Foraminiferal Microfossil Studies with Transfer Function (TF)**

Recent expansion of detailed microfossil studies with TF in Cascadia paleoseismology and improvements in the methods of data processing and analysis have enhanced the resolution of the estimates of coseismic subsidence due to ancient Cascadia earthquakes. These studies correlate fossil assemblages to an intertidal foraminiferal set of contemporary assemblages (Figure 2.2). Because the foraminiferal assemblages in the intertidal environment vary with elevation, a change of as little as 5 – 10 cm in a given site may produce a recognizable change in the foraminiferal assemblage. In the procedure of constructing a TF, contemporary foraminiferal assemblages are collected along transects in the intertidal environment near sampled paleoseismic sedimentary archives, and are used to define the living elevations of different species relative to mean sea level (optima and tolerance) (Figure 2.2a). The dataset of contemporary species is called a “training set”. By correlating to the training set, fossil foraminifera collected in the sediment samples can be used to reconstruct former sea levels (Figure 2.2c). There are two important requirements in constructing a TF. First, the training set must systematically sample the full range of intertidal environmental variables. Second, the fossil records must remain intact. The second requirement means that the fossil sample locations must be protected from erosion by ocean waves.

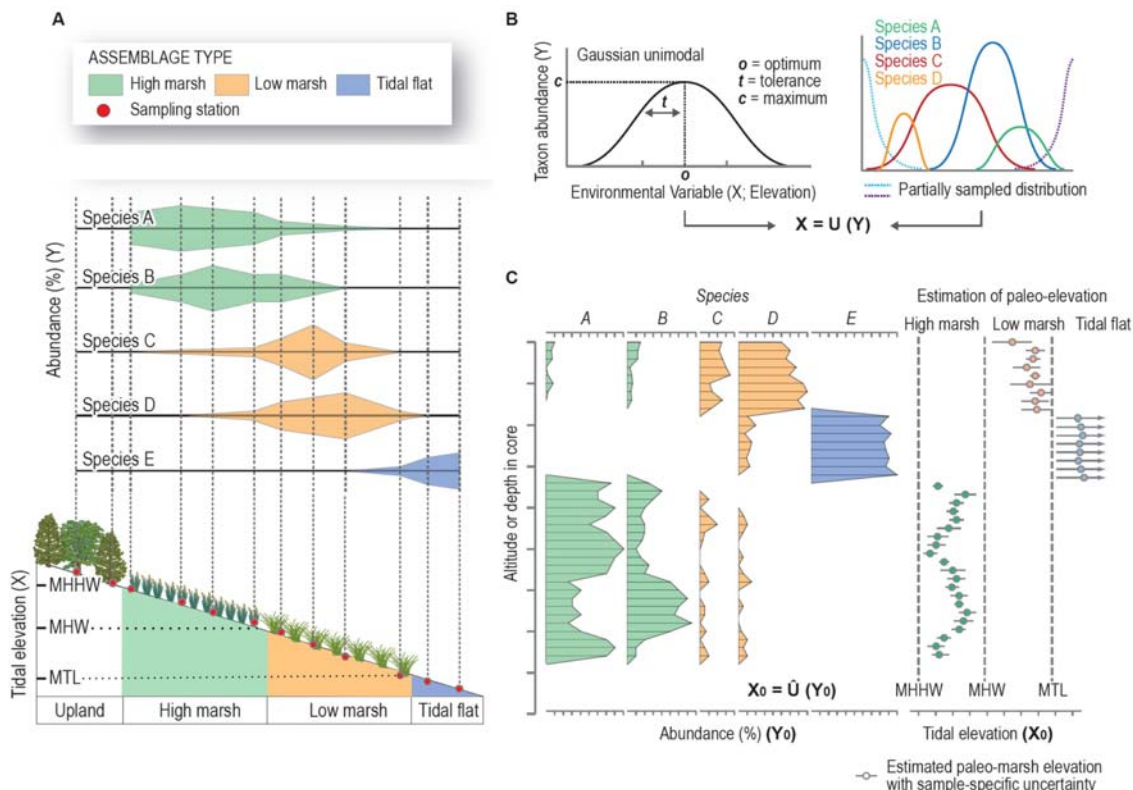


**Figure 2.2.** Developing a transfer function and correlating contemporary assemblages to fossil assemblages. (a) Constructing a training set through the full range of intertidal environments (bottom) and analyzing the abundance of different species (top). Species that live in a similar intertidal zone are grouped as the same assemblage. MHHW – mean high high water, MHW – mean high water, MTL – mean tide level. (b) Abundance of one species at different elevations, following a normal distribution (left), and the distribution of different species (right). Elevation (X) is expressed as an empirically derived function (U) of modern microfossils (Y). (c) The abundance of each species against depth in a sample core (left). Elevation of fossil species with respect to sea level is inferred from the distribution of contemporary species (right). Figure modified from *Horton et al.* [2012].

To construct a training set, contemporary foraminifera are identified and environmental variables are measured along intertidal transects across marshes at river-mouth estuaries (Figure 2.2a). In order to minimize the effect of environmental differences between the fossil and contemporary sites, the TF is constructed from a nearby modern transect no more than 150 m away from the fossil site. Defined by vascular plant species, shore-normal transects bisect five vertical floral zones comprising tidal flat, low marsh, middle marsh, high marsh, and forested upland [Eilers, 1975]. Contemporary foraminiferal species are sampled along shore-normal transects at short intervals through the full range of intertidal environmental variables [Birks, 1995]. The elevation of each sampling station is measured using an automatic level (Figure 2.3), and the relative elevations are tied into a local benchmark that gives absolute elevation with respect to the tide level. Although other environmental variables such as pore-water salinity, pH, and vegetation cover might control the distribution of the foraminiferal assemblages [e.g., Jonasson and Patterson, 1992; Goldstein and Watkins, 1999], Horton and Edwards [2006] found that elevation is the principal independent variable in controlling the distribution of foraminifera within the intertidal environment, because elevation directly controls the duration and frequency of tidal exposure [e.g., Horton, 1999; Horton and Edwards, 2006] and salinity [e.g., Jonasson and Patterson, 1992; Goldstein and Watkins, 1999].



**Figure 2.3.** Constructing a shore-normal training set from the upland to the tidal flat at Alsea Bay, Oregon. (a) Sampling stations are labelled with pink flags along the transit. Samples of the upper 1-cm of surface sediment are collected at each station. The elevation at each station is obtained by levelling. The coordinates and elevation of the benchmark are known from a nearby geodetic benchmark or by GPS. (b) Plant species are identified at each station as indicators to define vertical floral zones for the samples (photos taken by Pei-Ling Wang during the field work in coastal Oregon in April 2012).

To collect contemporary foraminifera, tens of samples are taken at each study site along a shore-normal transit. Samples are placed in vials with a calcium carbonate chip, rose Bengal (a protein staining agent), 30% ethanol water solution, and then refrigerated (Figure 2.4a). Rose Bengal is used to stain the living foraminifera and hence enable them to be differentiated from dead foraminifera. Because dead assemblages most accurately

reflect subsurface assemblages [Horton, 1999; Murray, 2000; Culver and Horton, 2005], foraminifera living at the time of collection are excluded. There are seven dominant agglutinated foraminiferal species in surface and subsurface environments along the Oregon coast (Figure 2.4b-f). In order to relate foraminiferal distribution to relative sea level and construct a modern TF, each sample requires 300 counts.

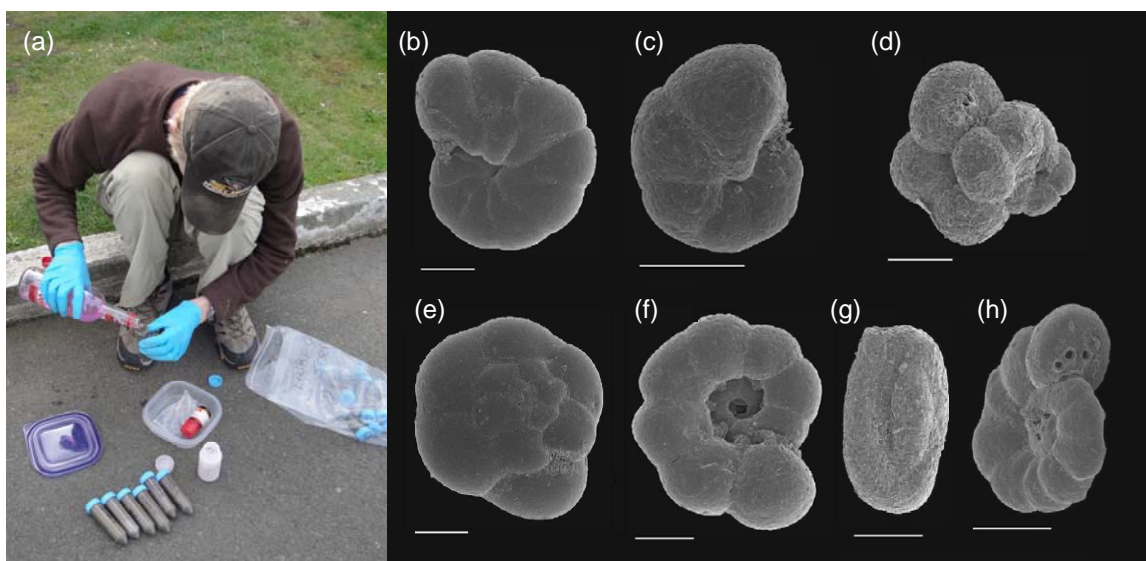


**Figure 2.4.** Processing foraminiferal samples in the field for identification of dominant agglutinated foraminiferal species in surface and subsurface sediment in Oregon intertidal environments [(b) through (h) modified from *Hawkes et al.*, 2010]. Scale bars equal 100  $\mu\text{m}$ . (a) Foraminifera samples are placed in vials with a calcium carbonate chip (in the white vessel), stained with rose Bengal (red vessel), then preserved in a 30% ethanol water solution (pink liquid in the glass bottle) (photo taken by Pei-Ling Wang during the field work in coastal Oregon in April 2012). (b) *Haplophragmoides manilaensis*. (c) *Haplophragmoides wilberti*. (d) *Trochammina irregularis*. (e) *Trochammina inflata*. (e) *Balticammina seudomacrescens*. (g) *Milliammina fusca*. (h) *Jadammina macrescens*.



**Figure 2.5.** Sampling of sediment sequences. (a) Taking Russian cores. (b) Storing the core sample in a plastic liner (photos taken by Pei-Ling Wang during the field work in coastal Oregon in April 2012).

Microfossils are sampled from sedimentary sequences that are collected from sediment cores or a cut-bank outcrop. Multiple sediment cores are taken using the method of Russian coring. Each core is 50-cm long, with a 10-cm overlap in sampling depth between the upper and lower sections (Figure 2.5). That is, the first core is from 0- to 50-cm deep, the second core is from 40- to 90 cm deep, the third core is from 80- to 130- cm deep, and so on. Because the color of the core samples will change due to drying and oxidization, the samples are immediately photographed (Figure 2.6). To minimize the color change, the samples are wrapped with plastic wrap. Compared to coring, a superior sampling method is collecting sediments from freshly excavated cut-bank outcrop (Figure

2.1b), because the overall strata can be clearly seen, and the samples suffer less distortion and contamination during sampling.



**Figure 2.6.** Taking samples from the outcrop at the bank of Lewis and Clark River. Samples are cleared and photographed right after collecting, then wrapped and labelled to avoid drying and oxidizing (photo taken by Pei-Ling Wang during the field work in coastal Oregon in April 2012).

After the field work, tens to hundreds of foraminiferal fossils are sampled in the laboratory above and below the uppermost contact of the uppermost buried marsh (Figure 2.2c), which represents the surface just prior to the 1700 Cascadia earthquake. The tsunami-deposited sand is not sampled for foraminifera because of the unstable sedimentation environment; the presence of assemblages in the tsunami sand that live only at elevations lower than the tidal marsh strongly indicates that the sand had been

transported landward, and that it is not an in situ intertidal deposit. The dominant species in the fossil assemblage collected through the sediment sequence at each site are correlated to the training set. By comparing microfossils from the sedimentary record with the contemporary assemblages (Figure 2.2c), we can estimate the paleo-elevation of fossil species prior to and after the earthquake-induced displacement. For all the study sites, a rapid increase in relative sea level based on the TF is interpreted as coseismic subsidence.

With the TF, the amount of coseismic coastal subsidence is more precisely constrained than with other methods [e.g., *Guilbault et al.*, 1996; *Horton and Edwards*, 2006]. Since TF provides a paleoelevation for every fossil sample in a sequence, the resolution is improved. When combined with lithostratigraphic data, the reconstructions of relative sea level before and after an earthquake typically have precisions in a range of  $\pm 0.1$ - $0.3$  m [e.g., *Guilbault et al.*, 1996; *Edwards et al.*, 2004; *Gehrel et al.*, 2005, 2008; *Horton and Edwards*, 2006]. The uncertainty, in terms of one standard deviation of a normal probability distribution (Figure 2.2b), is about 30 cm for the  $\sim 2.5$  m tidal range but would increase with larger tidal ranges [*Nelson et al.*, 1996a].

## **2.3. Microfossil Paleoseismic Observations Used in This Work**

### **2.3.1. Estimates from Transfer Function Analysis of Microfossil Data**

There is now a sufficient distribution of good-quality estimates of coseismic subsidence based on TF-assisted foraminiferal analyses to allow us to infer along-strike variations in megathrust slip in the 1700 earthquake. Fourteen TF estimates are available for this study, as listed in Table 2.1. Most of the TF estimates are from estuaries along the

Oregon coast; three of them are from the west coast of central Vancouver Island (Figure 2.7, Table 2.1).

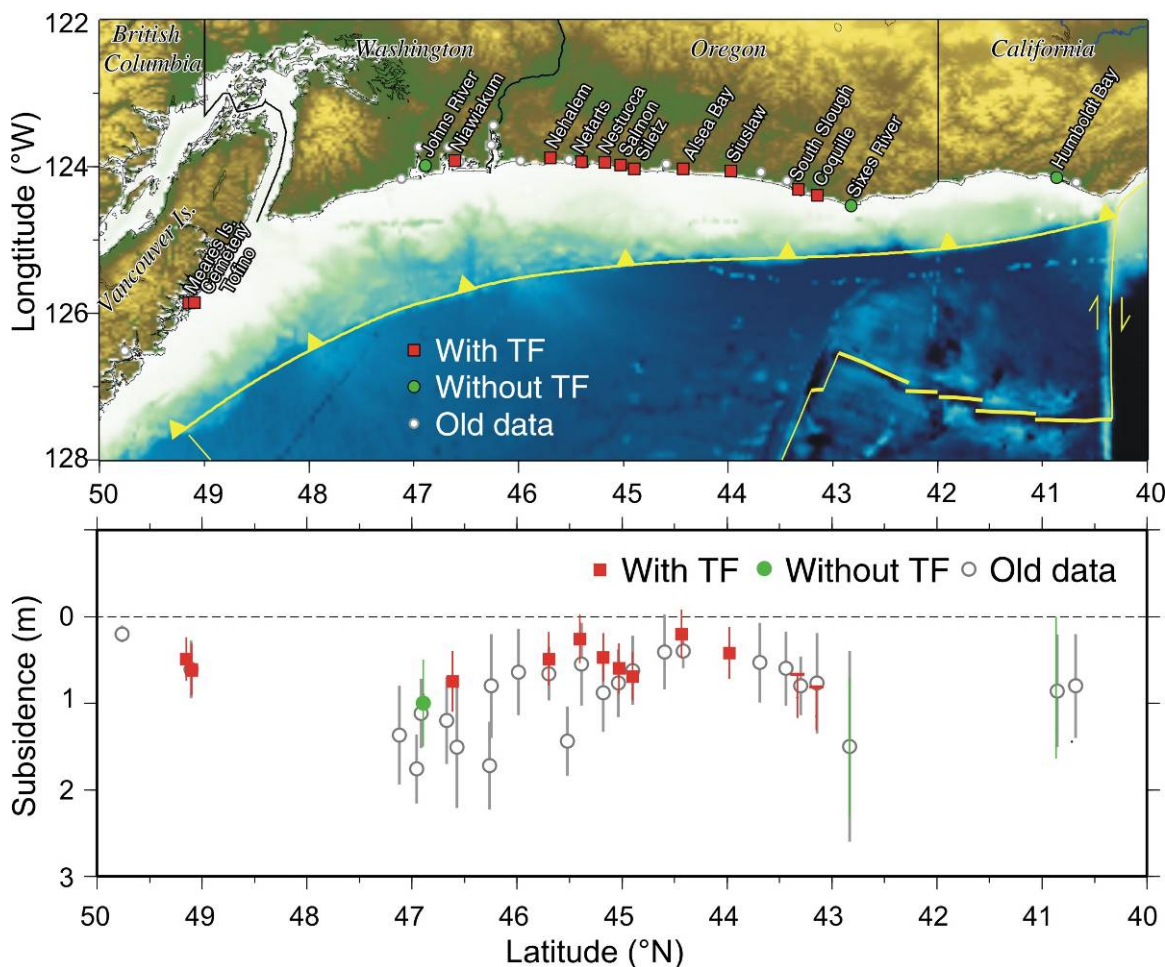


**Figure 2.7.** Previous paleoseismic studies (white circles) and microfossil studies used in this work (red symbols: with TF; green symbols: without TF). Old data are from *Leonard et al.* [2010] (details will be discussed in Section 3.3). (a) Spatial distribution of paleoseismic studies along the Cascadia margin. (b) Coseismic subsidence estimates. Uncertainties in the newer paleoseismic estimates (red and green symbols) are described as follows: symmetric error bars represent one standard deviation of normal probability distribution (Figure 2.2b), one-sided bars indicate minimum subsidence estimate, and a bar with no symbol indicates uniform distribution.

**Table 2.1** Paleoseismic estimates used in this study

Site	Latitude (°N)	Longitude (°W)	Subsidence (m)	Standard Deviation (m)	Probability Distribution	Method <sup>a</sup>	Reference	Remarks
<b>Vancouver Island</b>								
Meares Island	49.15	-125.86	0.49	± 0.25	Normal	TF	<i>Guilbault et al.</i> [1996]	No analogues in the modern data used to estimate the subsidence.
Cemetery	49.10	-125.85	0.62	± 0.29	Normal	TF	<i>Guilbault et al.</i> [1996]; <i>Hawkes</i> (unpublished)	Revised using a TF
Tofino	49.10	-125.85	0.61	± 0.30	Normal	TF	<i>Hughes et al.</i> [2002]	
<b>Washington</b>								
Johns River	46.89	-123.99	1.00	± 0.50	Normal	microfossil without TF	<i>Shennan et al.</i> [1996]	Used TWINSPLAN and detrended correspondence analysis to quantitatively compare fossil assemblages with modern assemblages.
Niawiakum	46.61	-123.92	0.75	± 0.35	Normal	TF	<i>Sabeau</i> [2004] (unpublished); <i>Hemphill-Haley</i> [1995]; <i>Atwater and Hemphill-Haley</i> [1997]	Combining reinterpretation of <i>Sabeau</i> [2004] unpublished data using new Oregon TF ( $0.57 \pm 0.33$ m) and estimate by <i>Hemphill-Haley</i> [1995], and <i>Atwater and Hemphill-Haley</i> [1997] ( $1.5 \pm 0.5$ m).
<b>Oregon</b>								
Nehalem	45.70	-123.88	0.49	± 0.31	Normal	TF	<i>Hawkes et al.</i> [2011]	

<sup>a</sup> TF: foraminiferal transfer function.

Table 2.1

Site	Latitude (°N)	Longitude (°W)	Subsidence (m)	Standard Deviation (m)	Probability Distribution	Method <sup>a</sup>	Reference	Description
Netarts Bay	45.40	-123.94	0.26	± 0.28	Normal	TF	<i>Engelhart et al.</i> (unpublished)	Used same methodology as <i>Hawkes et al.</i> [2011] with expanded modern dataset. In agreement with value obtained by semi-quantitative methods by <i>Shennan et al.</i> [1998].
Nestucca	45.18	-123.94	0.47	± 0.28	Normal	TF	<i>Hawkes et al.</i> [2011]	
Salmon	45.03	-123.98	0.60	± 0.29	Normal	TF	<i>Hawkes et al.</i> [2011]	
Siletz	44.90	-124.03	0.69	± 0.28	Normal	TF	<i>Engelhart et al.</i> (unpublished)	Used same methodology as <i>Hawkes et al.</i> [2011] with expanded modern dataset Flagged by author as possibly suspect due to taxonomy issues. <i>Nelson et al.</i> [2008] stated 0.40 ± 0.19 m but with problems due to no modern analogues.
Alsea Bay	44.43	-124.03	0.20	± 0.28	Normal	TF	<i>Engelhart et al.</i> (unpublished)	
Siuslaw	43.98	-124.06	0.42	± 0.30	Normal	TF	<i>Hawkes et al.</i> [2011]	
South Slough	43.33	-124.32	0.67	Minimum Estimate	asymmetric	TF	<i>Hawkes et al.</i> [2011]	Used same methodology as <i>Hawkes et al.</i> [2011] with expanded modern dataset
Coquille	43.15	-124.39	0.81	Minimum Estimate	asymmetric	TF	<i>Engelhart et al.</i> (unpublished)	
Sixes River	42.83	-124.54	1.50	± 0.80	Uniform	microfossil without TF	<i>Kelsey et al.</i> [1998]	
<b>California</b>								
Humboldt Bay	40.87	-124.15	0 - 1.64		Uniform	microfossil without TF	<i>Pritchard</i> [2004]	Use the Brackish Intertidal Diatom Index [BIDI, <i>Atwater &amp; Hemphill-Haley</i> , 1997]

<sup>a</sup> TF: foraminiferal transfer function.

Five of the coseismic estimates from Oregon are from *Hawkes et al.* [2010; 2011]. Using the same methodology as *Hawkes et al.* [2010], S. E. Engelhart and others (manuscript in preparation) acquired the three estimates at Netarts, Siletz, and Coquille. The sediment sequences at Alsea Bay studied by *Hawkes et al.* [2010] were re-sampled and the training set was reconstructed by Simon E. Engelhart, Alan R. Nelson, Robert C. Witter, and me during the fieldwork in Oregon in April 2012. The new estimate by *Engelhart et al.* (unpublished) is similar to that by *Hawkes et al.* [2010] and is used in this study. In southern Washington, *Hawkes et al.* (unpublished) re-evaluated the site of *Sabean* [2004] and taxonomically updated modern and fossil data by running these data through a regional or local TF (whichever provided the most matching analogues when comparing the modern and fossil assemblages). Estimates from Vancouver Island were obtained by *Guilbault et al.* [1996] and *Hughes et al.* [2002] but have been re-examined by Andrea D. Hawkes using a locally developed TF based on the modern data presented by *Guilbault et al.* [1996]. Revised results are listed in Table 2.1. At most of the TF sites, other types of paleoseismic estimates are either absent or of very poor quality and can be neglected.

The resolution of the subsidence estimate for each site is described using a probability distribution [*Hawkes et al.*, 2011]. The normal probability distribution is possible at sites where foraminiferal assemblages in the fossil record are present in similar abundances as the modern dataset (a ‘matching analogue’; *Hawkes et al.*, 2010) (Figure 2.2b). In some instances, foraminiferal assemblages are absent from the sediment deposited before the earthquake, and therefore only minimum estimates can be derived. For example, due to the paucity of available microfossils in the underlying peat layer (likely a forest soil), the

upper bound of the pre-seismic elevation at South Slough and Coquille sites could not be precisely defined. Therefore, the amount of subsidence is a minimum estimate. In this case, it is not possible to use a probability distribution to describe the uncertainties.

### **2.3.2. Estimates from Other Analyses of Microfossil Data**

To minimize data gaps along the subduction zone, each of the subsidence estimates compiled and used by *Leonard et al.* [2004; 2010] were re-evaluated by studying the original publications or analyzing the original datasets. The re-evaluation was carried out by our collaborators Alan R. Nelson, Simon E. Engelhart, Andrea D. Hawkes, and Benjamin P. Horton. In most cases, large errors made the subsidence estimates of minimal use for constraining along-strike variations of fault slip. In other cases, the estimates and their errors are very difficult to assess. However, this study includes subsidence estimates based on non-TF microfossil data from three sites, because these data are of relatively better quality and serve to fill some spatial data gaps (Table 2.1; Figure 2.7).

In southwest Washington (Johns River), *Shennan et al.* [1996] used detrended correspondence analysis to quantitatively compare fossil assemblages of pollen, diatoms, and foraminifers with modern assemblages of known elevation. These workers combined modern pollen and diatom data to define 7 environmental zones, 5 of them corresponding to tidal elevational zones. By using the analysis scores for fossil assemblages to assign them to one of the five elevational zones, *Shennan et al.* [1996] then calculated the maximum and minimum elevational changes across the contact marking subsidence during the 1700 earthquake. Using the ranges between maximum and minimum changes, *Shennan et al.* [1996] determined between 0.65 and 1.05 m of subsidence for one site and,

with greater uncertainty, 0.75 to 1.50 m for a second site 800 m downstream. Considering these two ranges and additional errors in the analysis that could not be quantified, *Shennan et al.* [1996] estimated subsidence in 1700 at  $1.0 \pm 0.5$  m for the Johns River site.

Along the southern Oregon coast (Sixes River), *Kelsey et al.* [1998] concluded that changes in diatom assemblages across the contact inferred to mark the 1700 earthquake are consistent with coseismic subsidence but are insufficient to estimate the amount of subsidence. However, in reconstructing the response of the Sixes River site to coseismic land-level change, these authors estimate that subsidence was at least 0.7 m and no more than 2.2 m (*Kelsey et al.*, 1998, their figure 4). We assumed that this range defines a uniform distribution with a mean of 1.5 m (Table 2.1).

At the southernmost site in Humboldt Bay (Figure 2.7), *Pritchard* [2004] used lithology and diatom assemblages to infer a sudden change from a low marsh environment to a tide flat across the abrupt contact marking the 1700 earthquake. By comparing the elevational ranges of pre-earthquake and post-earthquake environments in the same way as *Atwater and Hemphill-Haley* [1997], the subsidence is estimated at 0-1.64 m, with a uniform probability distribution.

## 2.4 Discussion

### 2.4.1 Uncertainties in Microfossil-based Paleo-elevation Reconstruction

The uncertainties in estimating amounts of subsidence during the 1700 earthquake from microfossil studies depend on a number of factors. In addition to the uncertainties due to the depth spread of the species (Section 2.1), other geological processes might also cause errors in paleo-elevation estimates. Possible sources include coseismic sediment compaction, and changes in tidal range after a change in the shape of the estuary.

Seismic shaking may cause compaction of the sediments. As observed in the 1964 Alaska earthquake, sediment compaction widely occurred [e.g., *Kachadoorian*, 1965; *Coulter and Migliaccio*, 1966; *Waller*, 1966; *Ovenshine et al.* 1976]. *Ovenshine et al.* [1976] reported that the 2.4 m subsidence in Portage area, south Alaska includes 0.8 m local compaction. If coseismic sediment compaction occurred during the 1700 Cascadia earthquake, observed coastal coseismic subsidence would be greater than tectonic subsidence due to elastic deformation alone. That is, subsidence estimated from paleoseismic studies may overestimate the actual elevation change due to the earthquake. However, there are arguments against significant sediment compaction during the great 1700 earthquake. *Guibault et al.* [1995] proposed that coseismic compaction near Tofino on west-central Vancouver Island would likely be small because the sediment layer is thin and overlies compact glaciomarine clay. *Guilbault et al.* [1995] also pointed out that there are no systematic differences in sediment thickness between sites that are close to bedrock outcrops and sites that are further away.

Changes in the shape of a river estuary after the earthquake may change the tidal range in the intertidal areas. Formation of barrier bars or spits may impede water exchange between river passage and the open ocean, thus changing the distribution of intertidal

species. *Guibault et al.* [1995] reported trees along the shoreline of Browning Passage in Vancouver Island that are at least 250 years old, which indicate that the sea level has not been higher than the present level over this time period. However, in southwest Washington, *Atwater and Yamaguchi* [1991] and *Atwater* [1992] found young dead trees in the intertidal zone, which indicates that significant transgression has taken place in the study region. In this study, I assume errors due to changes in the shape of estuaries are much smaller than the coseismic elevation change.

#### **2.4.2 Temporal Resolution of Paleoseismic Observations**

Paleoseismic studies show evidence for sudden coastal subsidence that is most likely due to prehistoric earthquakes. However, these studies can only define the “suddenness” to within months to years. Therefore, paleoseismic estimates of coseismic subsidence may be contaminated by postseismic deformation. Postseismic erosion and taphonomic alteration of microfossils can further degrade the temporal resolution [*Guilbault et al.*, 1996]. If the coast continued to subside for a few months or years following the earthquake, the microfossil analyses may overestimate coseismic subsidence. If the postseismic deformation was opposite of coseismic, the microfossil analyses may underestimate coseismic subsidence. If the postseismic motion reverses direction a short time after the earthquake, then the microfossil analyses may either over- or underestimate the coseismic subsidence. Modeling of subduction earthquakes shows that postseismic deep fault slip might increase subsidence at central Oregon, whereas uplift from viscoelastic relaxation might reduce the subsidence [*Hyndman et al.*, 2005; *Wang*, 2007].

Observations following recent subduction earthquakes have not offered a clear pattern of post-seismic motion. After the 1964 Alaska earthquake, areas of coseismic subsidence

were seen to be uplifting a few years after the earthquake [Cohen and Freymueller, 2001]. However, after the 2011 Tohoku earthquakes, some of the coastal areas that underwent coseismic subsidence have continued to subside (<http://www.gsi.go.jp/chibankansi/chikakukansi40005.html>; in Japanese), although it is possible that they may reverse their sense of motion in the near future.

Signs of postseismic deformation after the 1700 Cascadia earthquake have been seen in stratigraphic records. *Guibault et al.* [1996] studied two sites at Vancouver Island and reported strong microfossil and pollen evidence for postseismic rebound in the sediment layer on top of the buried peat or tsunami sand. *Hughes et al.* [2002] also inferred a rapid uplift rate from fossil pollen deposited on Vancouver Island following the 1700 Cascadia earthquake. From microfossil-based land-level changes, *Nelson et al.* [2008] inferred significant high rates of postseismic uplift at Alsea Bay, Oregon.

Paleoseismic studies assume postseismic vertical motion is much smaller than coseismic, such that the microfossil analyses yield mainly the coseismic component. If different parts of the Cascadia margin exhibit similar postseismic behavior, then errors in the paleoseismic estimates due to postseismic motion, especially those based on the same method of analysis, should be systematic and should not seriously affect the study of along-strike variations of coseismic slip. If the postseismic deformation also exhibit heterogeneous, the effect could be small assuming sediments overlay the peat layer deposit soon after coseismic elevation change. Improving the temporal resolution of “coseismic” elevation changes remains an important issue of paleoseismic research.

#### **2.4.3 Incompleteness of Paleoseismic Observations**

The model to be developed in this work is limited by the spatial distribution of

paleoseismic studies. The distribution is determined by the spatial extension of tidal wetlands suitable for recording the coseismic change. For the use of TF, as mentioned in Section 2.2, a full intertidal environment from forest upland to tidal flat is required. But such an environment is not present everywhere along the Cascadia margin. In northern Washington, there is a lack of paleoseismic evidence for sudden elevation change, although the reason is currently unknown. If this area experienced coseismic uplift in 1700, a scenario that will be discussed in Section 5.4, peat-mud or peat-sand couplets are unlikely to be found in the intertidal zone. In northern California, because of the rocky coastal areas, few sites are available for paleoseismic studies (Figure 2.7). My models are not well constrained in these regions where data gaps occur.

## Chapter 3. Previous Work in Cascadia Megathrust

### Rupture Simulation

#### 3.1. Thermal Constraints to the Seismogenic Zone

*Hyndman and Wang* [1993; 1995] inferred the updip and downdip limits of the seismogenic zone for Cascadia from heat flow data and thermal modeling along four profiles (Figure 3.1a). They proposed that the fault becomes seismogenic where the temperature is higher than 150°C and lower than about 350°. Within this temperature range, the fault is assumed to exhibit a velocity-weakening behavior and, thus, is expected to be locked during the interseismic period. If warmer than 350-450°C, the fault is assumed to exhibit stable-sliding (Figure 3.1a). At even higher temperatures, fault zone material probably deforms ductilely and is unable to store enough elastic strain energy to produce earthquakes.

The width of the thermally defined seismogenic zone varies along the Cascadia margin due mainly to variations in the dip of the plate interface (Figure 1.1). Compared with other subduction zones, the width of the thermally defined seismogenic zone at Cascadia is narrow, because the incoming oceanic plate is young (thus hot) and covered roughly by a 3-km thick insulating layer of sediment. The updip limit of the thermally defined seismogenic zone is assumed to be at the deformation front, where the temperature at the top of the incoming igneous crust is well above 150°. The downdip extent is located at a relatively shallow depth, about 15-25 km corresponding to the temperature range of 350°C to 450°C along the plate interface [*Oleskevich et al.*, 1999]

(Figure 3.1).

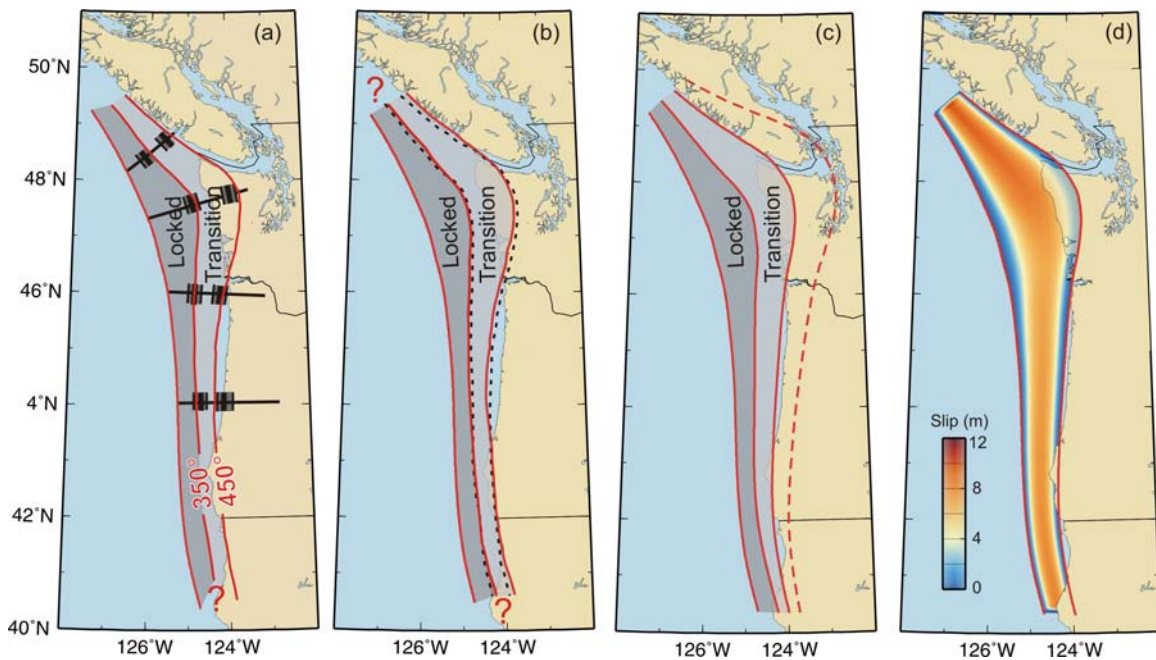


**Figure 3.1.** Updip and downdip limits of seismogenic zone in Cascadia defined by various studies (Red lines). (a) Interseismically locked and transition zones suggested by Hyndman and Wang [1995] (modified from Hyndman and Wang [1995]). Black lines are deformation model profiles constrained by thermal analysis (thick short lines) and GPS observations (stippled areas). (b) Interseismic model of Flick et al. [1997] (modified from Flick et al. [1997]). Black dashed lines show estimated widths by Hyndman and Wang [1995]. (c) Interseismic model of Wang et al. [2003]. Red dashed line defines the downdip limit of the effective interseismic transition zone (ETZ). The locked zone was used as the full-slip zone and the seaward half of the ETZ used as the linear transition zone in the coseismic model of Wang et al. [2003] and Satake et al. [2003]. (d) A coseismic rupture model similar to Priest et al. [2009]. Slip on the plate interface follows a bell-shape function to be discussed in Section 3.3.

### 3.2. Models of Interseismic Locking

The current state of interseismic locking of the Cascadia megathrust has been inferred from geodetic observations. Long-term tide gauge records, repeated levelling surveys, triangulation and trilateration measurements, and Global Positioning System (GPS) measurements have been used to constrain elastic models of interseismic locking [e.g., *Savage et al.*, 1991; *Dragert et al.* 1994; *Dragert and Hyndman*, 1995; *Hyndman and Wang*, 1995; *Burgette et al.*, 2009]. Early models of Cascadia interseismic deformation were two-dimensional (2-D) and were developed along margin-normal cross sections assuming a planar megathrust fault (Figure 3.1a). *Dragert et al.* [1994] and *Hyndman and Wang* [1995] used a fully locked segment and incorporated a deeper zone of transition from full locking to slipping at the plate convergence rate (Figure 3.2).

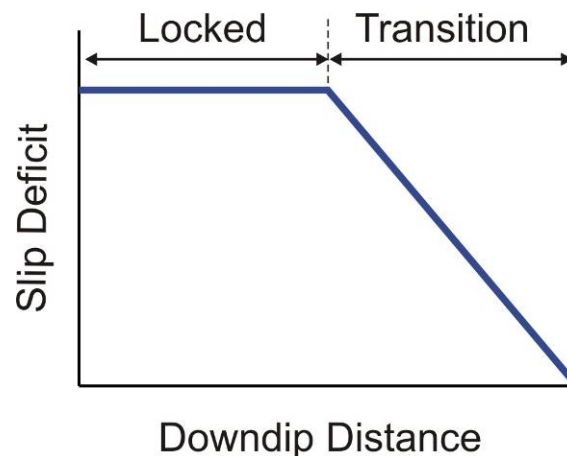


**Figure 3.2.** Slip deficit (backslip) distribution in the locked and transition zones.

*Flück et al.* [1997] developed a three-dimensional (3-D) elastic dislocation model. They constructed a 3-D curved fault by compiling and extrapolating seismic-survey observations and intraslab earthquake distributions. They also invoked thermally defined

locked and transition zones as in *Hyndman and Wang* [1995] but slightly adjusted the widths of these zones to optimize the fit to levelling observations (Figure 3.1b). In this model, they assumed a uniform convergence rate of 42 mm/yr with a constant direction along the margin. The distribution of the locked and transition zones (Figure 3.1b) in their solution is similar to that of the 2-D model of *Hyndman and Wang* [1995] (Figure 3.1a).

Using the same fault geometry as *Flück et al.* [1997], *Wang et al.* [2003] developed a 3-D model with a very wide “effective transition zone” (ETZ) that partially accounts for the effect of viscoelastic stress relaxation during the interseismic period (Figure 3.1c). The width of the locked zone was still assumed to be thermally controlled, while the width of the transition zone was adjusted to fit geodetic strain rates and GPS velocities (Figure 3.1c). However, *Wang et al.* [2003] pointed out that the model of interseismic locking should not be regarded as a mirror image of coseismic rupture. In estimating fault locking, they used the relative convergence between the subducting Juan de Fuca (JDF) plate and the Cascadia forearc instead of the North America (NA) plate, based on the forearc motion model of *Wells et al.* [1998] and *Wells and Simpson* [2001] (Figure 3.3). Compared with JDF-NA convergence, the direction of JDF-forearc convergence is less oblique and shows less along-strike variation in its margin-normal component (Figure 3.4).

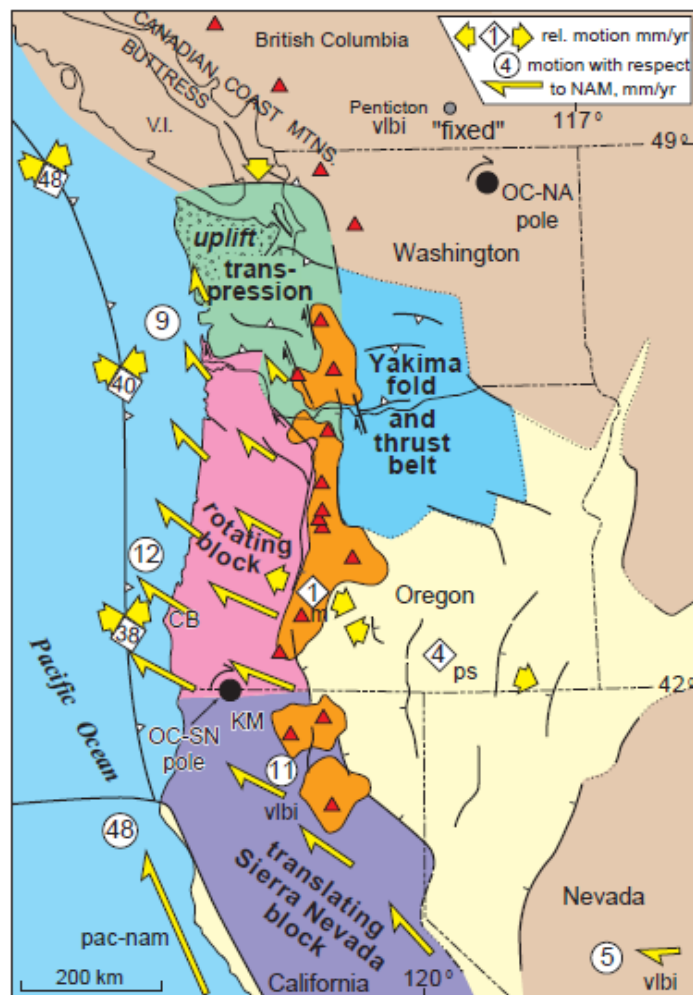


**Figure 3.3.** Fore-arc motion model of Wells *et al.* [1998] and Wells and Simpson [2001] (from Wells and Simpson [2001]). Cascadia forearc is divided into Washington (W), Oregon Coastal (OC), and Sierra Nevada (SN) blocks. Yellow half arrows on the OC block are fore-arc motion rates relative to SN block and defined by the OC-SN Euler pole in Klamath Mountains (KM). The rotation of OC block deforms W block and causes north-south compression and uplift. Paired yellow arrows show relative motion; rates (mm/yr) are given by diamonds.

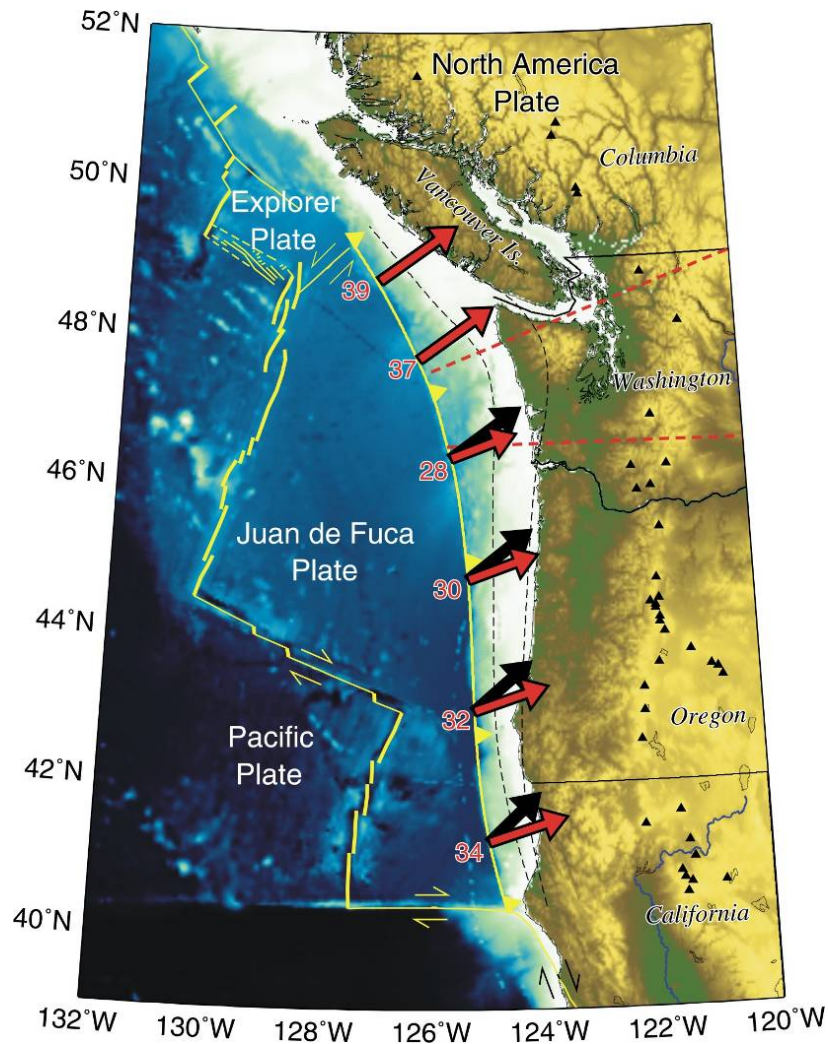


**Figure 3.4.** Correction of forearc rotation. Black arrows: JDF – North America plate convergence vectors. Red arrows: JDF – Cascadia forearc convergence based on the model of *Wells and Simpson* [2001]. Black dashed lines represent previously used downdip limits of uniform coseismic slip zone and linear transition zone, corresponding roughly to the 350°C and 450°C isotherms, respectively, defined by *Wang et al.* [2003] and similar to *Hyndman and Wang* [1995] and *Flück et al.* [1997]. Black triangles denote volcanoes. Euler poles for the relative plate motions are given in Chapter 4 and explained in *Wang et al.* [2003]. Red dashed lines divide the fault into three portions subject to different Euler poles, i.e., the northern section is subject to the JDF-NA pole; the southern section is subject to the JDF-forearc pole. The central portion is a linear transition zone from one model to the other.

There are other types of interseismic models for Cascadia, some of which have been reviewed by *Wang* [2007]. The most notable is the elastic model of interseismic locking inferred by inverting a large number of GPS velocities by *McCaffrey et al.* [2007]. In this work, *McCaffrey et al.* [2007] simultaneously determined the locking state of the megathrust and the Euler vectors of a number of upper-plate blocks, allowing a large number of degrees of freedom. The validity of the block boundaries and the effects of including the block motion on the inferred megathrust locking are difficult to assess. There is also a class of Cascadia megathrust deformation models that employs a viscoelastic Earth [*Wang et al.*, 2001, 2012]. These models illustrate the importance of viscoelastic stress relaxation of the asthenospheric mantle in affecting interseismic deformation, and hence reinforce the idea that coseismic and interseismic deformation are not mirror images of each other.

### 3.3. Models of Coseismic Deformation

For the Cascadia megathrust, the only constraints for coseismic slip in past great earthquakes are paleoseismic and paleotsunami observations. *Flück et al.* [1997] modeled coseismic deformation by reversing interseismic deformation, that is, the interseismic fully locked zone became a zone of full slip, while the interseismic transition zone became the coseismic downdip transition from full to zero slip (Figure 3.1b). They pointed out the need for future comparison with paleoseismic data.

To model coseismic deformation, *Wang et al.* [2003] used a shallow full-rupture zone plus a downdip transition zone much narrower than the ETZ used in their interseismic

model (Figure 3.1c). The downdip end of their coseismic transition zone is similar to that of *Flück et al.* [1997] (Figure 3.1b), which is roughly the 450°C temperature contour estimated by *Hyndman and Wang* [1995] by extrapolating from three 2-D thermal-modeling profiles crossing northern and central Cascadia (Figure 3.1a). With a rupture uniformly recovering a 500-yr slip deficit of JDF-forearc convergence along the full length of the margin, the model predicted a subsidence pattern that was generally consistent with the few, then available, paleoseismic observations for the Cascadia earthquake of 1700 deemed to be reasonably reliable by these authors.

To explain the height of tsunami waves that reached Japan in 1700, *Satake et al.* [2003] adopted the 3-D model of *Wang et al.* [2003] (Figure 3.1c) and tested different rupture widths and a scenario in which the rupture at the updip end was diverted to a splay fault. These models represented earthquakes of magnitudes M 8.7 - 9.2. The shorter the rupture length along strike, the larger was the slip required to match the observed tsunami heights. However, full-length rupture models appeared to be more consistent with the paleoseismic coastal subsidence observations along the Cascadia margin.

*Leonard et al.* [2004; 2010] modified previous 3-D models to explain various paleoseismic observations, also with a full-rupture zone plus a linear transition zone. Their preferred model was similar to the “Long-Narrow” model of *Satake et al.* [2003]. However, in calculating slip deficit to be recovered by an earthquake, they did not use a uniform convergence vector as in *Flück et al.* [1997] or the JDF-forearc convergence as in *Wang et al.* [2003] and *Satake et al.* [2003]. Instead, they used the JDF-NA convergence (black arrows in Figure 3.4).

*Leonard et al.* [2004; 2010] compiled previous estimates of coseismic subsidence to

constrain their model. Because these estimates often show large scatter, *Leonard et al.* [2010] strove to use as much information as possible from as many sites as possible. They compiled qualitative-to-quantitative subsidence values based on field and lab data collected by tens of investigators using different methods and assumptions over 15 years. Because the variable quality of the data resulted in large scatter and errors in subsidence estimates from the same or nearby sites, *Leonard et al.* [2010] weighted estimates based on inferred data quality and summarized them with moving-average values along the subduction zone. The weights were assigned based on factors that were considered to affect the quality of the subsidence estimates, such as the method used (qualitative, semi-quantitative, or quantitative; lithology vs. microfossil, etc.), number of sites or samples analyzed, the number of estimates at the same site, and the precision of estimated errors. Estimates based on microfossil assemblages were given the highest weight, whereas estimates based on lithologic changes alone were assigned the lowest. Because of the large errors on the original data and the qualitative factors considered in weighting it, *Leonard et al.*'s [2010] average subsidence estimates resulted in large scatter and errors in the site-average estimates (old data in Figure 2.6), and thus cannot be used to construct a rupture model with along-strike variations.

*Priest et al.* [2009] adopted the curved fault geometry proposed by *McCrorry et al.* [2004] for simulation of tsunami sources. The model of *Priest et al.* [2009] (Figure 3.1d) differed from all previous rupture models for Cascadia in that it did not use a uniform rupture zone plus a linear transition zone, called the "linear function" here (Figure 3.5), to prescribe downdip slip distribution. Instead, it adopted the bell-shape function proposed by *Wang and He* [2008] (Figure 3.5) based on the earlier work of *Freund and Barnett*

[1976]. The tapering of slip both updip and downdip in the bell-shape function is more consistent with the observed slip distribution in earthquakes and predictions of slip by rupture mechanics. For this reason, I choose to use the bell-shape function in my present modeling. However, details of the slip distribution in the dip direction, especially those of the updip end, are of no importance in modeling coastal subsidence. Modeling the impact of tsunami waves on local coasts is different because the details of the shallow slip distribution are of first-order importance. *Priest et al.* [2009] also considered two models involving along-strike heterogeneous slip, but only for their sensitivity tests. In my present work, heterogeneous slip is the focus of investigation.

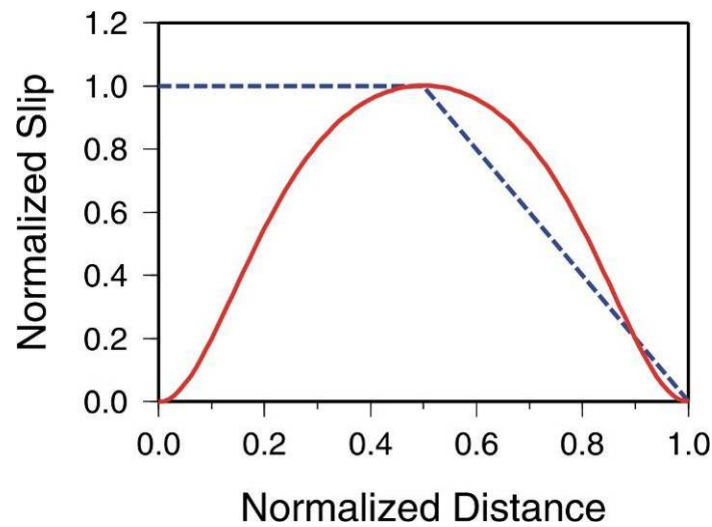


**Figure 3.5.** Two types of downdip distribution of coseismic slip. Linear slip function (blue dashed line) and bell-shape function of *Wang and He* [2008] (red solid line).

## Chapter 4. Modelling Method

### 4.1. Basic Assumptions

In this study, I follow the same modeling strategy as *Priest et al.* [2009] but focus on along-strike variations of coseismic slip. Several assumptions have been made on the fault geometry, rupture extent, slip magnitude, and slip direction.

The 3-D fault geometry is exactly that of *McCrorry et al.* [2004] (Figure 1.1) with no simplifications. However, because the model is developed for an elastic half-space that has a flat surface, it cannot include the actual topographic and bathymetric reliefs. For simulating surface deformation caused by fault slip, what is important is depth below the free surface (ground surface and seafloor), not depth below sea level. Therefore, a trivial correction to the geometry of the shallow part of the fault is made so that the fault depth below the flat model surface approximately represents depth below the seafloor and ground surface in the real Earth [*Flück et al.*, 1997; *Wang et al.*, 2003]. Other details of the 3-D dislocation model will be explained in the next section.

Because all the paleoseismic observations are located on the coast (Figure 2.2), for each latitude there is only one data point in the strike-normal direction. Thus, the updip and downdip terminations of the seismogenic zone cannot be independently constrained by presently available paleoseismic observations. Following previous works reviewed in Chapter 3, I assume that the rupture is confined between the deformation front and the 450°C isotherm (Figure 3.1). For testing the hypothesis of variable slip along-strike, the downdip limit is not a critical parameter, but I nonetheless test model sensitivity to the downdip rupture width.

The direction of coseismic slip is assumed to be in the reverse direction of JDF-forearc convergence (Figure 3.4) as in *Wang et al.* [2003] and *Priest et al.* [2009]. Specifically, the JDF-forearc motion is described using two Euler poles (Table 4.1). Two straight lines divide the fault mesh into south, central, and north regions, as shown in Figure 3.4. From southern Washington southward, the Euler pole for JDF-forearc convergence was based on the forearc-NA convergence of *Wells and Simpson* [2001]. In northernmost Cascadia, that is, British Columbia, the JDF-forearc convergence is described simply by the JDF-NA pole. In the area in between, that is, northern Washington, a linear transition between the two convergence fields is assumed (Figure 3.2).

**Table 4.1** Euler poles used in this study (from *Wang et al.*, [2003])

Pole	Latitude (°N)	Longitude (°E)	Rotation Rate (°/Ma)
JDF-NA	26.63	-110.45	-0.804
JDF-forearc	67.40	-147.94	0.627

## 4.2. 3-D Dislocation Model

Coseismic surface deformation is simulated with a 3-D numerical dislocation model in an elastic half space. The modeling code “Disl3d” includes the point-source dislocation solution of *Okada* [1985] and a set of subprograms that were developed by Kelin Wang. The subprograms allow users to construct a slab surface, define a fault mesh with interconnected triangular elements along the slab surface, and assign slip patches to the fault mesh. An example of the fault mesh is shown in Figure 4.1.

The core of the dislocation program is calculating the point-source solution for surface displacement. *Okada* [1985; 1992] developed a set of analytical expressions for surface displacement and strain for point and rectangular sources. *Disl3d* numerically integrates the point-source solutions to obtain surface displacements at any point on the surface. A slip vector is assigned to each of the triangular elements of the fault mesh to represent a point dislocation source. Deformation of the top surface of the model is the sum of all the point-source dislocation solutions over the entire fault mesh [*Flück et al.*, 1997; *Wang et al.*, 2003]. Vertical displacements are calculated at the locations of paleoseismic observations, so that the model results can be compared to the coseismic subsidence estimates derived from these observations. The Poisson's ratio is set to be 0.25. For a uniform half-space, no other material properties are needed.

The earthquake magnitude is calculated from the scalar seismic moment ( $M_0$ ), which is defined by

$$M_0 = \mu AD \quad (4-1)$$

where  $\mu$  is the shear modulus,  $A$  is the rupture area, and  $D$  is the average slip. The moment magnitude is defined as [*Hanks and Kanamori*, 1979]

$$M_w = \log_{10}(M_0 - 9.1) / 1.5. \quad (4-2)$$

The moment magnitude of the model earthquake should be close to 9, to be consistent with 1700 tsunami wave heights in Japan [*Satake et al.*, 2003].

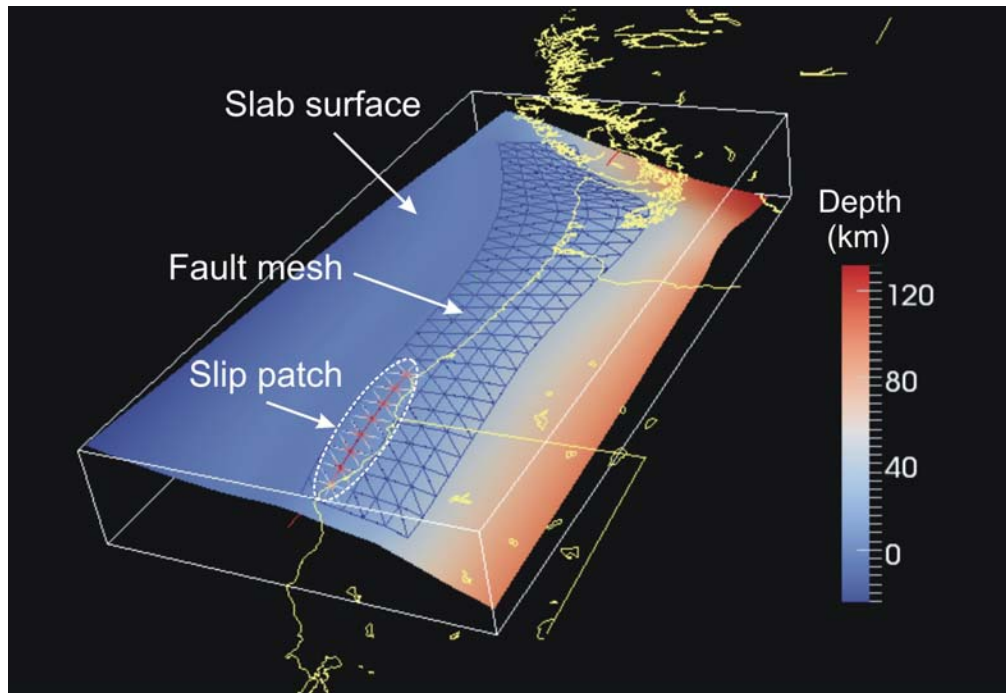


**Figure 4.1.** Structures of slab surface, fault mesh, and slip patch in the model. The fault mesh is about 1000-km long and 300-km wide. The density of the triangular elements on the fault mesh is reduced for clarify.

### 4.3. Slip Distribution

Slip on the fault mesh is assigned using slip patches (Figure 4.1). In this study, I define the shape and the location of slip patches based on a trial-and-error approach (details discussed in Section 4.4). On each patch, the magnitude of peak slip is assigned as the plate convergence rate multiplied by a period of time that represents the equivalent time of slip deficit accumulation. The relative plate motion is as described in Section 4.1 above.

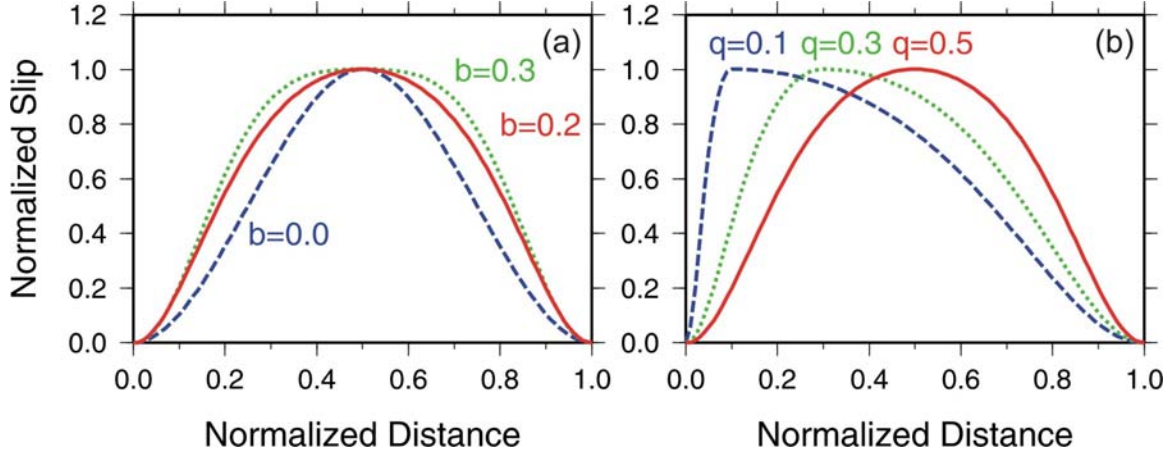


**Figure 4.2.** Slip distributions with different values of broadness  $b$  and skewness  $q$ . (a)

When the broadness parameter  $b=0$ , the peak or the slip distribution is narrower than crack model predictions. A broadness value of 0.2 fits the distributions predicted by crack mechanics. (b) When the skewness parameter  $q=0.5$ , the slip distribution is symmetric. When  $q<0.5$ , the peak slip is skewed updip. If  $q>0.5$ , the peak slip would be skewed downdip.

Fault slip in the slip patches of my heterogeneous rupture models is assumed to follow the bell-shape function (Figure 4.2) in the downdip direction as proposed by *Wang and He* [2008] and applied by *Priest et al.* [2009]. The function is reproduced as follows

$$s(x') = s_0 \delta(x') \{1 + \sin[\pi \delta(x')]\}^b, \quad (4-3a)$$

$$\delta(x') = \begin{cases} \frac{6}{q^3} x'^2 \left( \frac{q}{2} - \frac{x'}{3} \right) & 0 \leq x' \leq q \\ \frac{6}{(1-q)^3} (1-x')^2 \left( \frac{1-q}{2} - \frac{1-x'}{3} \right) & q \leq x' \leq 1 \end{cases} \quad (4-3b)$$

with  $x' = x/W$ , where  $x$  is downdip distance from the upper edge of the rupture zone, and

$W$  is local downdip width (Figure 4.3). The skewness parameter  $q$  ranges from 0 to 1, and the broadness parameter  $b$  ranges from 0 to 0.3. Examples of various  $b$  and  $q$  values are shown in Figure 4.2. In this study, I use  $b=0.2$  and  $q=0.5$ ; the slip peaks in the middle of the patch in the dip direction.

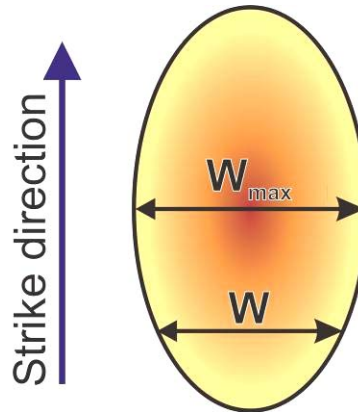


**Figure 4.3.** Definition of the local width ( $W$ ) and maximum width ( $W_{\max}$ ) of a slip patch.

The most important issue to investigate in this study is along-strike slip variation. As mentioned in the Introduction, slip in great earthquakes often consists of areas of high slip separated by areas of low slip. In this work, I represent high-slip areas in the simplest way, that is, as elliptical patches in which the slip peaks at the center and tapers toward the edge in all directions. The major axis of each ellipse is set to be approximately parallel to the local strike direction of the subduction fault (Figure 4.3). Where the margin geometry does not allow simple assignment of elliptical patches, such as the concave seaward corner off southern Vancouver Island and the Olympic Peninsula, or where the paleoseismic data are difficult to fit with such simple patch shape, I let the patches

deviate from the elliptical shape. The slip magnitude is quadratically scaled with the local width of the slip patch  $((W/W_{\max})^2$ , see Figure 4.3). Thus, there is less slip where the width of the patch is less than the widest part.

#### 4.4. Modeling Procedure

I use a trial-and-error approach and adjust various model parameters such as the size, location, and peak slip for various patches and the number of patches by comparing model predictions with paleoseismic subsidence estimates. As explained in Section 4.1, slip patches are located within the thermally defined seismogenic zone (Figure 3.1). To fit shorter-wavelength variations of coastal subsidence along strike, I introduce low slip areas to divide a larger slip patch into smaller ones. These low-slip areas are also referred to as “segmentation boundaries”, but I do not imply that these are necessarily persistent features that rupture in the same way in successive great earthquakes. Slip parameters will be given in characterizing the various models discussed in the next chapter.

Despite my efforts to gather as many microfossil-based subsidence estimates as possible, there are still two large data gaps in northern and southern Cascadia, as discussed in Section 2.4.3. For these areas of no data, I do not arbitrarily introduce “segmentation boundaries” except for testing purposes. Therefore my preferred model necessarily features large size of slip patches in these areas. Future paleoseismic observations from these areas may change the rupture model.

## Chapter 5. Model Results

### 5.1. Uniform-Slip Models

I first constructed two models of uniform slip to see how they compare with the recent, more precise subsidence estimates (Figure 5.1). Here, as in *Wang et al.* [2003], *Satake et al.* [2003], and *Leonard et al.* [2004], “uniform” means the equivalent time of slip-deficit accumulated and recovered by the coseismic slip is constant in the strike direction along the entire margin. In the rest of the thesis, the amount of coseismic slip is always measured in terms of the equivalent time of slip-deficit accumulation. For example, a 500-yr slip means 20 m if the local convergence rate is 40 mm/yr, but 15 m if the local convergence rate is 30 mm/yr.

These two uniform-slip models differ in the downdip distribution of coseismic fault slip. One of them (Figure 5.1a) has the classical “linear” distribution illustrated in Figure 3.5. The other (Figure 5.1b) has the bell-shape distribution illustrated in Figure 4.2. Figure 5.1c shows subsidence values at the paleoseismic observation sites predicted by these two models.

The model of linear downdip distribution with 500-year slip is similar to the model of *Leonard et al.* [2004; 2010] (Figure 5.1a). However, as mentioned in section 3.3, *Leonard et al.* [2004; 2010] used JDF-NA instead of JDF-forearc convergence rate and direction. As a result, the margin-normal component of the coseismic slip off southern Oregon and northern California was quite small (see Figure 3.4) and fortuitously fitted the limited paleoseismic data (gray circles in Figure 5.1c). Had the JDF-forearc convergence been used, the model with 500-year slip would have substantially over-predicted coseismic

subsidence in this area, as shown by the dotted line in Figure 5.1c.

A 300-year slip for the linear distribution or 250-year slip for the bell-shape distribution can roughly fit the general trend of the paleoseismically estimated coastal subsidence. The peak slip in the bell-shape model is located more landward than in the linear model (Figure 3.5), and hence the bell-shape model requires slightly less slip to fit the coseismic coastal subsidence. The similarity of the results from these two models (Figure 5.1c) illustrates the insensitivity of the coastal subsidence to details of the downdip distribution of fault slip.

Although the uniform-slip models can roughly explain the trend of paleoseismic estimates, they do a poorer job explaining the second-order shorter-wavelength variations. One way to improve the fit to the paleoseismic estimates is to vary the downdip extent of the rupture zone. For example, we can modify the model of Figure 5.1a in this fashion to produce the model shown in Figure 5.2a. However, although this model can fit the paleoseismic estimates rather well (Figure 5.2b), the assumption of uniform slip, i.e. the same slip deficit time along strike, is unrealistic as discussed in Chapter 1. In the following sections, I present more realistic models featuring non-uniform slip in the strike direction.

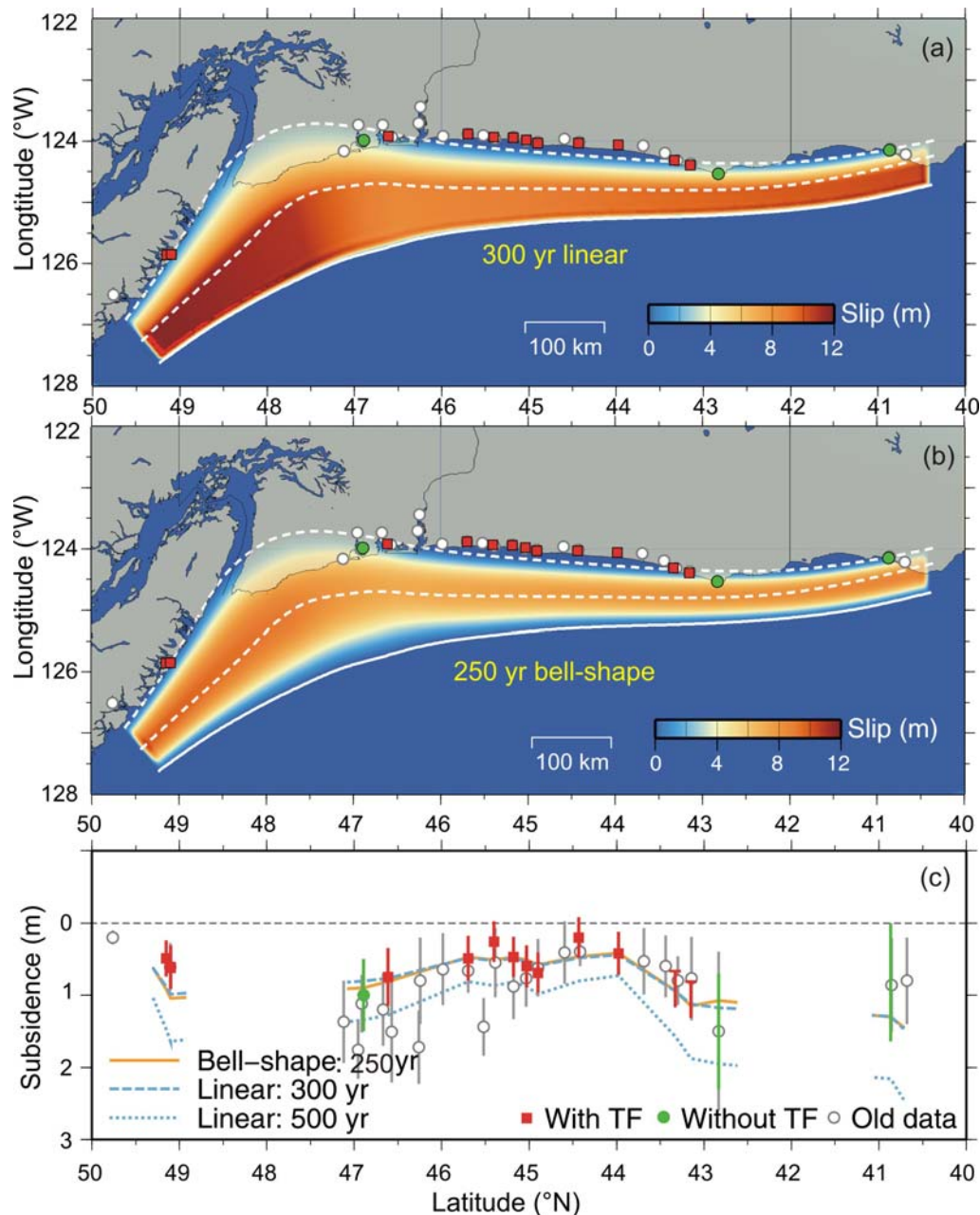


**Figure 5.1.** Models of uniform slip along-strike (in terms of equivalent time of slip-deficit accumulation). (a) Linear down-dip slip distribution with slip equivalent to 300 years of slip-deficit accumulation at current rate of JDF-forearc and JDF-NA (in northern Cascadia) convergence. The white dashed lines delineate the down-dip limits of the full slip zone and transition zone. Sites of paleoseismic observations are color-coded as in (c). (b) Bell-shape slip distribution with 250-yr slip. Other symbols are the same as in (a). (c) Model-predicted subsidence in comparison with paleoseismic estimates. TF: subsidence estimates derived from a microfossil transfer function. Older estimates, mostly based on non-microfossil data, used by *Leonard et al.* [2004; 2010] are shown as gray circles. The 500-yr slip model with linear distribution is similar to that used by *Leonard et al.* [2004; 2010].

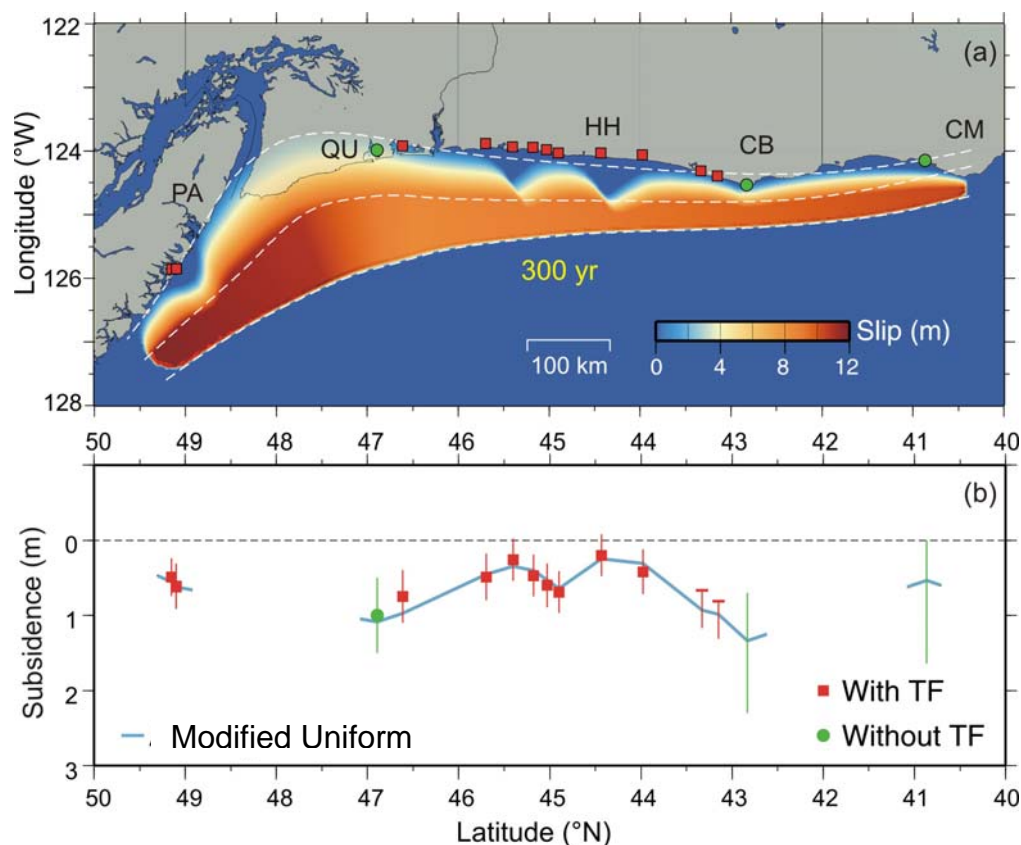


**Figure 5.2.** A model modified from that shown in Figure 5.1a by varying the downdip extent of the rupture limit. (a) Slip distribution. The white dashed lines are the same as that in Figure 5.1. PA – Port Alberni, QU – Quinault, HH – Heceta Head, CB – Cape Blanco, CM – Cape Mendocino. (b) Model subsidence at the observation sites.

## 5.2. Preferred Model

Consistent with observations of subduction earthquakes (see Section 1.3), I propose a model of multiple high-slip patches for the 1700 great Cascadia earthquake (Figure 5.3a). In this model, I let the slip taper updip to become zero at the deformation front. The slip in all the patches peaks offshore and drops off towards the coast except for the northernmost patch that extends further landward (Figure 5.3a). Perspective views of the slip distribution on the fault and related vertical deformation of the surface are shown in

Figure 5.4. Surface deformation is also plotted along three margin-normal profiles (Figure 5.5). The total rupture area on the fault is about  $9.94 \times 10^{10} \text{ km}^2$ , and  $M_w = 8.9$  (Table 5.1). Because radiocarbon dating of subsidence contacts dates past earthquakes to only a century or two (rarely to several decades), or months in the case of tree-ring data for the 1700 event [Yamaguchi *et al.* 1997; Jacoby *et al.*, 1997], the slip patches shown in Figure 5.3a could be interpreted as a sequence of smaller earthquakes over decades to a century. However, the scenario of all the patches rupturing in the same great earthquake is more consistent with the heights of the tsunami waves observed in Japan in 1700 [Satake *et al.*, 2003]. Also, there are no other smaller tsunami events in the Japanese historical records around that time that can be identified as due to a smaller Cascadia earthquake.

Compared to the uniform-slip models (Figure 5.1c), the preferred model fits the paleoseismic estimates in central Cascadia much better (Figure 5.3c). Although the uniform-slip model appears to fit the data within the uncertainties, the model predictions are less likely to fit the sites at Netart and Alsea Bay, because the estimate at each site has a normal probability distribution. Obviously, the slip in the northernmost and southernmost patches is nearly unconstrained because of the lack of paleoseismic observations in these areas. In particular, the slip off northern California and the continuity of slip distribution off Washington and British Columbia should be viewed with considerable caution. The two existing microfossil-based subsidence estimates at Cape Blanco (CB) and Cape Mendocino (CM) did not involve TF and thus have very large uncertainties. I assume a value of 450-yr, the average of the 200 - 700 yr range (the shading area in Figure 5.3c), for the southernmost patch.

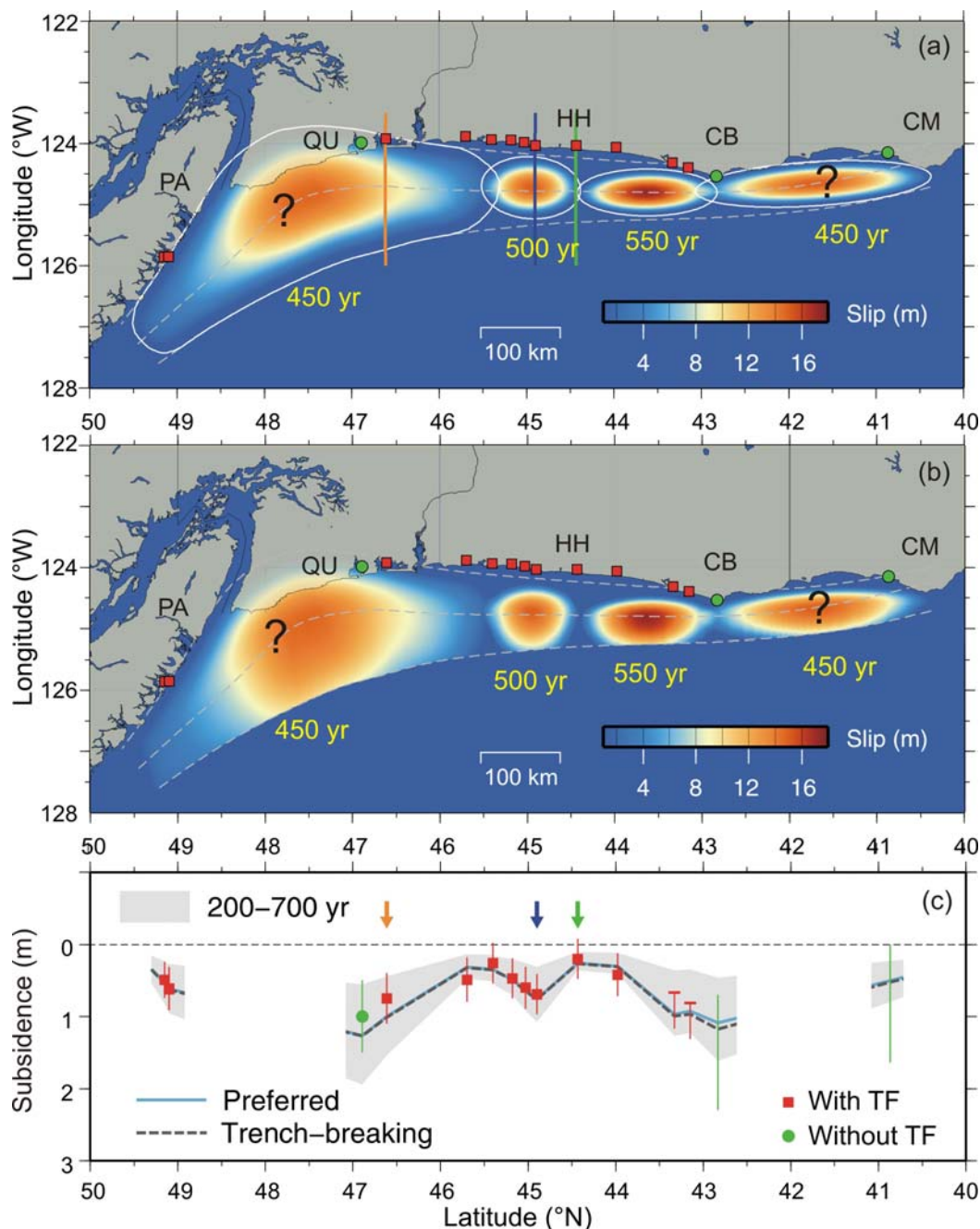


**Figure 5.3.** The preferred model and a trench-breaking rupture model for the 1700 Cascadia earthquake. (a) Slip distribution of the preferred model consisting of high-moment slip patches delineated by white lines. Peak slip (warmest color) labelled for each patch is measured in terms of equivalent time of slip-deficit accumulation. The gray dashed lines are the same as the white dashed lines in Figure 5.1. Deformation along the three margin-normal profiles is shown in Figure 5.5. PA – Port Alberni, QU – Quinault, HH – Heceta Head, CB – Cape Blanco, CM – Cape Mendocino. (b) Slip distribution of the trench-breaking rupture model. (c) Model-predicted coseismic subsidence in comparison with paleoseismic estimates. The shaded area is bounded by results for bell-function uniform slip (Figure 5.3a) of 200 yr and 700 yr.

The “segmentation boundary” at about 44.5°N is needed because paleoseismic data from this area (Alsea Bay, Oregon) indicate little subsidence (Figure 5.3c). The boundary near 45.5°N (near Netarts Bay) is introduced in order to explain the short-wavelength along-strike variations in coastal subsidence in this area. The third boundary, around 43°N (off Sixes River near Cape Blanco), is introduced mainly to explain the potentially large subsidence at 42.83°N. Although this boundary may not be well constrained by the data, *Witter et al.* [2003] inferred that some earthquake ruptures were limited by a segmentation boundary at Cape Blanco, because paleoseismic records varied to the north and south of this latitude.

The boundaries do find support from apparent correlation with other geological and geophysical observations or inferences. For example, near the low-slip area offshore of Alsea Bay (~ 44.5°N), there is a reported subducting seamount [*Trehu et al.*, 2008]. *Wang and Bilek* [2011] suggested that subducting seamounts should create an unfavourable condition for large seismic slip and act as barriers during a great earthquake. Several studies have proposed a segmentation boundary at Cape Blanco near 43°N. *Goldfinger et al.* [2012] postulated that the Blanco Fracture Zone and pseudofaults on the incoming plate may give rise to a segment boundary. Using large-scale ambient noise tomography, *Porritt et al.* [2011] proposed a strong shear velocity contrast in this area. Both the Heceta Head and Cape Blanco boundaries (Figure 5.3) roughly coincide with boundaries of offshore basins inferred from gravity lows by *Wells et al.* [2003]. These segmentation boundaries in the model need to be tested by future, more densely spaced paleoseismic observations.

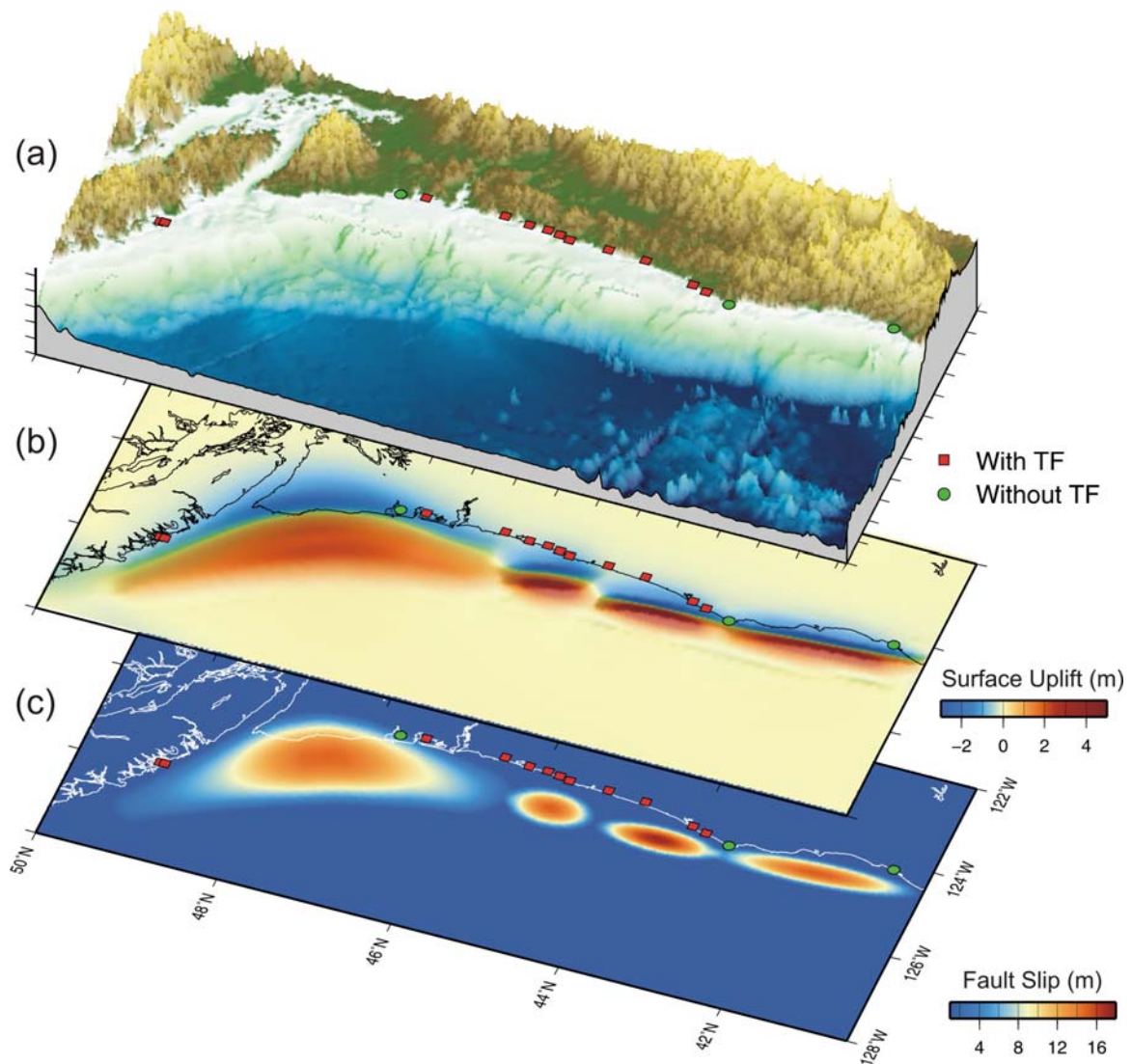


**Figure 5.4.** Topography, surface deformation, and fault slip distribution of the preferred model. (a) The 3-D Topography of Cascadia margin and spatial distribution of paleoseismic observations. (b) Model-predicted surface deformation. (c) Fault slip distribution of the preferred model.

**Table 5.1.** Slip parameters and earthquake magnitudes of different models

<b>Model</b>	<b>Figure</b>	<b>Peak Slip<sup>a</sup> (years)</b>	<b>Area (km<sup>2</sup>)</b>	<b>Moment (N m)</b>	<b>M<sub>w</sub></b>
Linear Uniform	5.1a, c	300	1.13E+11	3.11 +22	8.9
	5.1c	500	1.13E+11	5.18E+22	9.1
Bell-shape Uniform	5.1b, c	250	1.13E+11	2.18E+22	8.8
Modified Uniform	5.2	300	1.04E+11	2.96E+22	8.9
Preferred	5.3a,c	450, 400, 550, 450	9.94E+10	2.45E+22	8.9
Trench-breaking	5.3b, c	450, 400, 550, 450	1.94E+11	3.16E+22	8.9
Wide	5.6a, b	450, 400, 550, 450	1.17E+11	2.84E+22	8.9
	5.6a, b				
Wide-200	5.8	250, 200, 350, 250	1.17E+11	1.16E+22	8.7
Narrow	5.6a, c	450, 400, 550, 450	8.71E+10	2.06E+22	8.8
	5.6a, c				
Narrow+200	5.8	650, 600, 750, 650	8.71E+10	2.95E+22	8.9
Two-patch	5.9	450, 300	1.06E+11	2.13E+22	8.8
	5.9	450, 500	1.06E+11	2.42E+22	8.9
Eight-patch	5.9	450, 450, 500, 500,	7.58E+10	1.87E+22	8.8
		550, 500, 500, 500			

<sup>a</sup> Slip is measured in terms of recovered slip deficit accumulated over a time period.

For multiple high-slip patches, the peak values are listed from north to south.

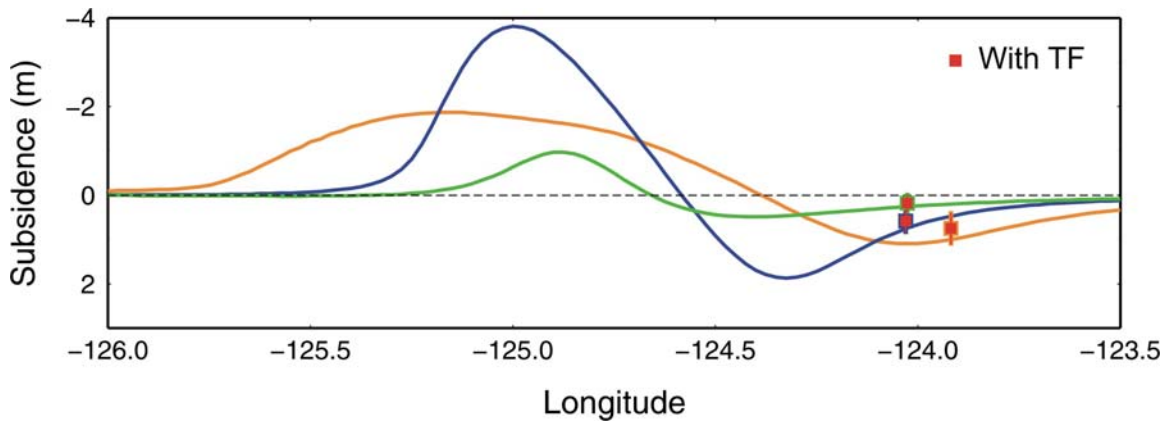


**Figure 5.5.** Predicted vertical motions for the preferred model, along margin-normal profiles, and the nearest paleoseismic estimates (outlined with the same color as the nearby profile). Colour-coded profile locations are shown in Figure 5.3a.

### 5.3. “Trench”-Breaking Rupture

During the 2011 M 9.0 Tohoku earthquake in Japan, very large trench-breaking rupture occurred, as is inferred from repeat multibeam bathymetric surveys off the Sendai coast [Fujiwara *et al*, 2011]. Although the shallowest portion of the megathrust is generally believed to have a velocity-strengthening behavior that tends to impede slip, whether it can prevent trench-breaking rupture depends on the degree of its coseismic strengthening and the size of the earthquake [Hu and Wang, 2008], especially if dynamic weakening is involved [e.g., Hirose and Bystricky, 2007]. It is not yet clear whether very large slip at the trench is a general feature of the Tohoku rupture or is limited to a relatively small area. Nor is it known whether this behavior is common in all subduction zones. Nonetheless, it is possible that the 1700 Cascadia earthquake might have exhibited a similar rupture behavior that may or may not be as dramatic as in the Tohoku event.

This possibility may have important implications for the mechanism of tsunami generation.

To account for the possibility of trench-breaking rupture, I modified the preferred model to produce a model in which the slip does not become zero at the deformation front (Figure 5.3b). Although the Cascadia subduction zone does not have a bathymetric trench because of the large amount of sediment, I still call this model the “trench-breaking” rupture model. The downdip half of the slip patches is the same as in the preferred model, but the updip half is stretched 50% seaward and truncated by the deformation front (Figure 5.3b). The moment magnitude is about M 9.0. The model-predicted coastal subsidence is nearly identical with the preferred model (Figure 5.3c). The magnitude of the trench-breaking earthquake can be further increased by assigning even larger slip near the trench, unless countered by a lower value of the shear modulus (as may be expected at shallower depths [*Bilek and Lay, 1999*]), but the coseismic coastal subsidence will be little affected. Unless the trench-coast distance is very small, coastal subsidence estimates contain no information on the rupture behavior of the most updip portion of the megathrust rupture. The conclusion of this test is simply that Cascadia paleoseismic observations do not presently rule out trench-breaking rupture.

#### 5.4. Trade-off between Rupture Width and Slip Magnitude

This set of models is designed to test the effect of downdip rupture width. Figure 5.6 displays some model results out of many tests. The along-strike slip distribution and the positions of the updip boundaries of the slip patches are identical to those of the preferred model (Figure 5.6a). To produce wider or narrower ruptures, the lower boundaries of the patches are moved landward or seaward by 30%, respectively (Figure 5.6a).

With the same peak slip as in the preferred model, the Wide model generally results in larger coastal subsidence than the preferred model (Figure 5.6b). A 200-year reduction in slip reduces the subsidence and better fits most of the paleoseismic estimates. On the other hand, with the same peak slip as the preferred model, the Narrow model results in smaller subsidence than the preferred model (Figure 5.6c). A 200-year increase in slip can better fit the paleoseismic data (Figure 5.6c), but the slip (650-750 yr) is too large when compared to the average recurrence interval of great Cascadia earthquakes of about 500 years although not impossible considering the full recurrence range of 200-1000 years. Therefore, there are two main conclusions from these tests: as discussed in Section 4.1. First, downdip rupture width and slip magnitude cannot be independently inferred from coastal subsidence observations. Second, ruptures much narrower than the preferred model with correspondingly larger slip appear to be less realistic than somewhat wider ruptures with smaller slip.

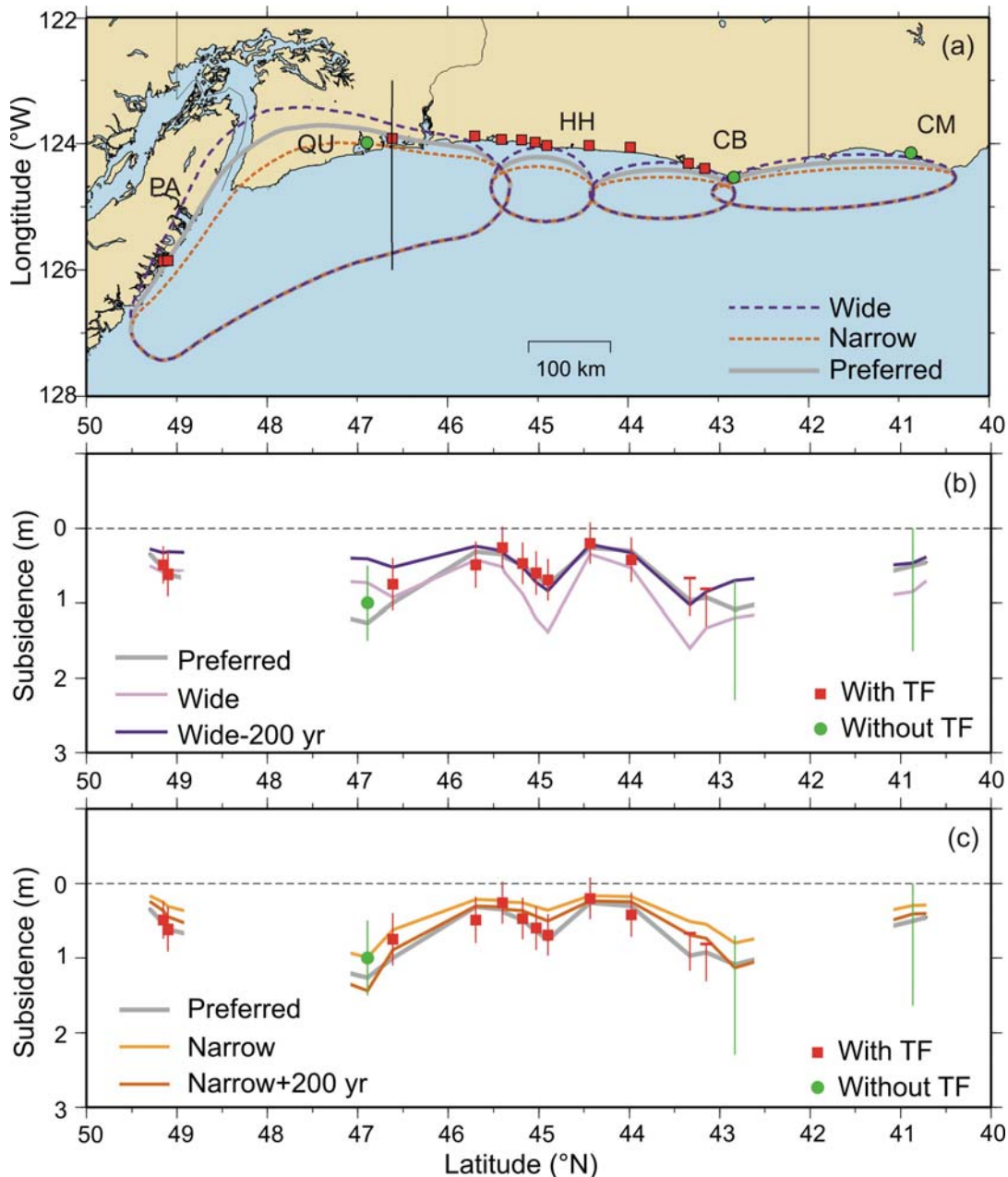


**Figure 5.6.** Tests for the effects of different downdip rupture widths. (a) Outlines of high-slip patches (slip distribution is similar to that shown in Figure 5.3a). The seaward boundary is fixed. For Wide and Narrow models, the downdip width is increased or decreased by 30% from the preferred model of Figure 5.3a. Deformation along the margin-normal profile is shown in Figure 5.7. PA – Port Alberni, QU – Quinault, HH – Heceta Head, CB – Cape Blanco, CM – Cape Mendocino. (b) Model subsidence for wider ruptures. In the Wide model, peak slip is the same as that of the preferred model. In the Wide-200 model, the peak slip for each patch is that of the preferred model minus 200 years. (c) Model subsidence for narrower ruptures. In the Narrow model, the peak slip is the same as the preferred model. In the Narrow+200 model, the peak slip for each patch is that of the preferred model plus 200 years.

The subsidence patterns produced by the Wide-200 and Narrow+200 models can be better explained using a margin-normal displacement profile (Figure 5.7). Because there is only one paleoseismic data point for each profile, models with various widths can all fit the datum by changing the slip magnitude. If the rupture width increases, the wavelength of the surface deformation increases (blue dashed line), and vice versa (orange dotted line). To produce the same subsidence on the coast, a wider rupture requires smaller slip, while a narrower rupture requires large slip. However, increasing patch width does not always increase coastal subsidence. It depends on the location of the coast relative to the location of the peak subsidence. If the coast is seaward of the peak subsidence, moving the downdip boundary of the rupture patch landward will decrease, not increase, coastal subsidence. This is what happens between the preferred and the Wide model around latitude 47°N (Figure 5.6b).

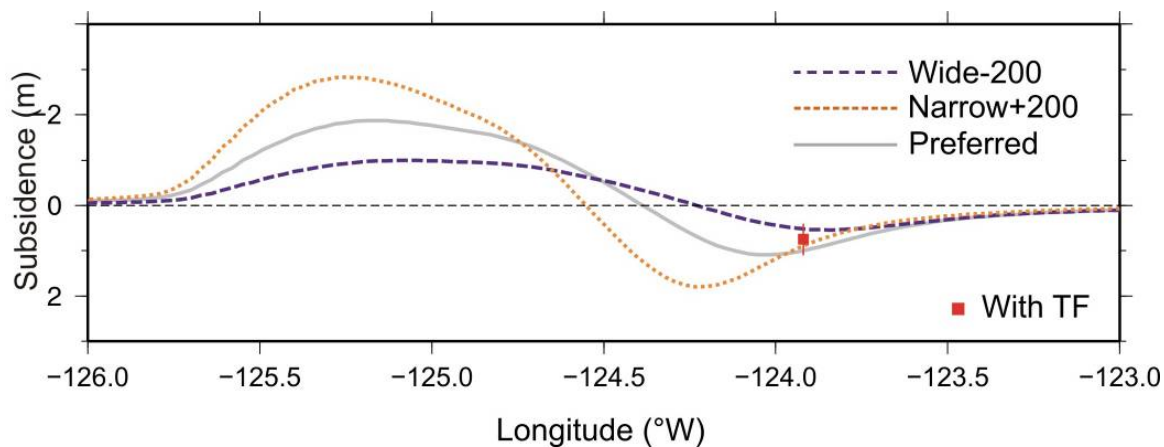


**Figure 5.7.** Model-predicted vertical motion for the Preferred, Wide-200, and Narrow+200 yr models along the margin-normal profile shown in Figure 5.6a and the nearest paleoseismic estimate.

Figure 5.8 shows the map view of surface deformation predicted by the Narrow+200, preferred, and Wide-200 models. The downdip expansion of the rupture area causes a landward shift of the “hinge line”, the boundary between areas of coseismic uplift and subsidence, and the narrowing of the rupture causes a seaward shift. This affects not only the magnitude of coastal subsidence, but also the polarity of coseismic deformation in some regions. For example, in the coastal area of northern Washington, the Narrow+200 model (Figure 5.8a) predicts greater subsidence than does the preferred model (Figure 5.8b). The model-predicted surface deformation in this region changes from subsidence to uplift in the Wide-200 model (Figure 5.8c). However, due to the paucity of paleoseismic observations in this region, the rupture extent cannot be constrained. If the coastal area of northern Washington underwent coseismic uplift, no coseismic subsidence evidence would be recorded in the sediment sequences in intertidal marsh environments. It is possible, but more difficult, to record evidence of coseismic uplift, e.g., as at Cape Mendocino. A detailed comparison of coseismic coastal deformation predicted by various models in areas where paleoseismic observation is absent is given in Section 5.6.1.

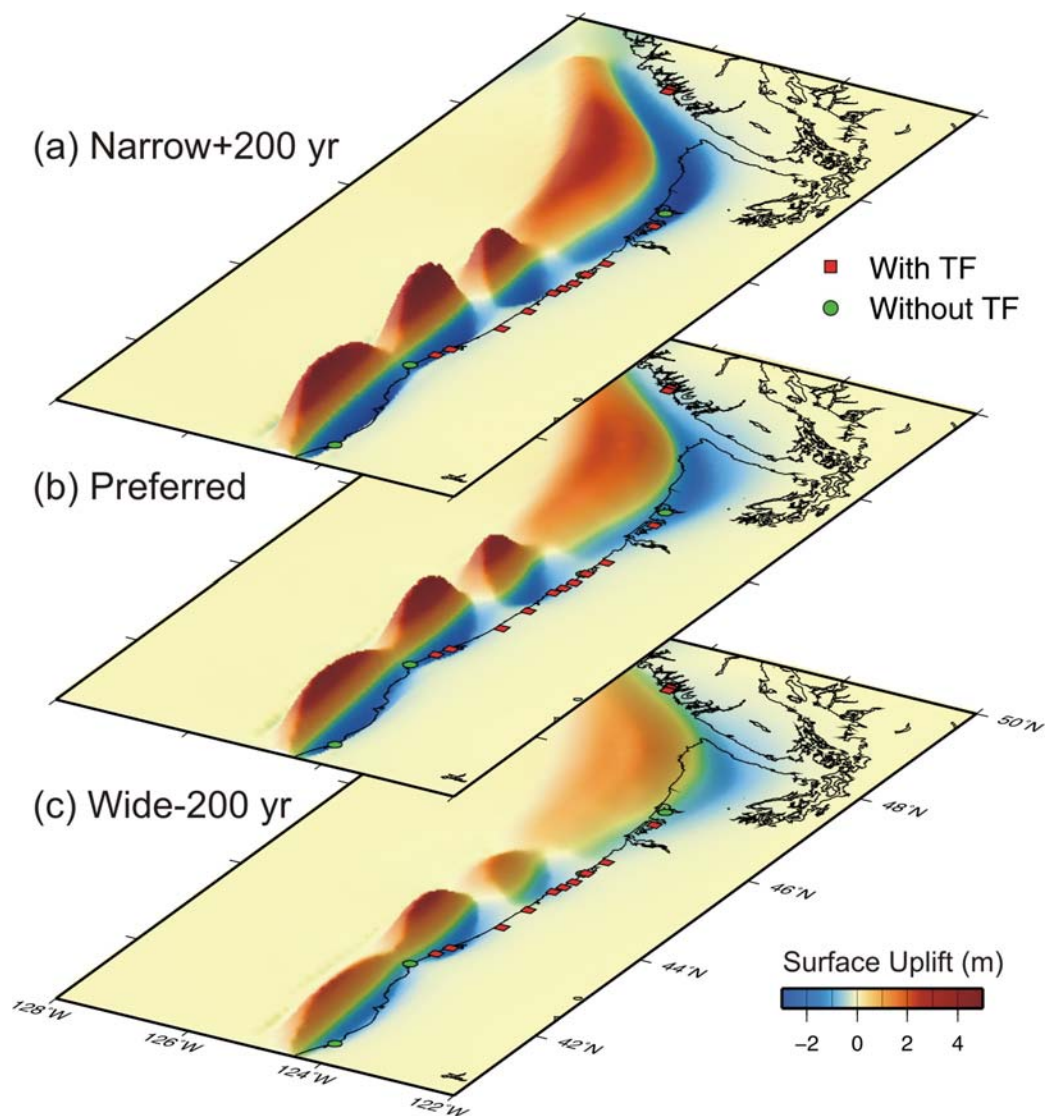


**Figure 5.8.** Comparison of surface uplift magnitude and distribution, for models with different downdip rupture widths and slip. (a) The Narrow+200 model. (b) The preferred model. (c) The Wide-200 model.

## 5.5. Other Scenarios of Along-strike Variations

To illustrate the effect of low-slip areas on surface deformation and to explain how I introduced the three segmentation boundaries shown in Figure 5.3a, I show two test models with different numbers of slip patches. The model parameters are shown in Table 5.1. For these tests, I let the slip taper to zero at the deformation front as in the preferred model, but the conclusions do not change if I use a trench-breaking scenario instead.

The first test is a two-patch model (Table 5.1, Figure 5.9a). The segmentation boundary off Alsea Bay is the same as in the preferred model and hence can explain the low subsidence in this area. However, with only one segmentation boundary, this model cannot explain the short-wavelength variations of coastal subsidence near 45°N (Figure 5.9b); hence another boundary is needed at ~45.5 N. If the peak slip of the southern patch is 300 years, the model-predicted subsidence at 42.83°N may be too small (Figure 5.9b). If the slip is increased to 500 years, the model better fits the paleoseismic estimate at 42.83°N but greatly over-predicts subsidence at ~43.2°N (Figure 5.9b). This example better explains why three segment boundaries are needed by the preferred model (see Section 5.2).

A second test is an eight-patch model. It is motivated by the interesting observation that some of the segmentation boundaries in my preferred model are in agreement with boundaries of offshore basins inferred from gravity lows by *Wells et al.* [2003]. The eight-patch model is constructed by dividing the northernmost and southernmost high-slip patches of the preferred model each into three smaller patches roughly according to the distribution of seven forearc basins (Figure 5.9a). As shown in Figure 5.9b, where paleoseismic observations are available, this model predicts a subsidence pattern similar

to the preferred model (Figure 5.3c).

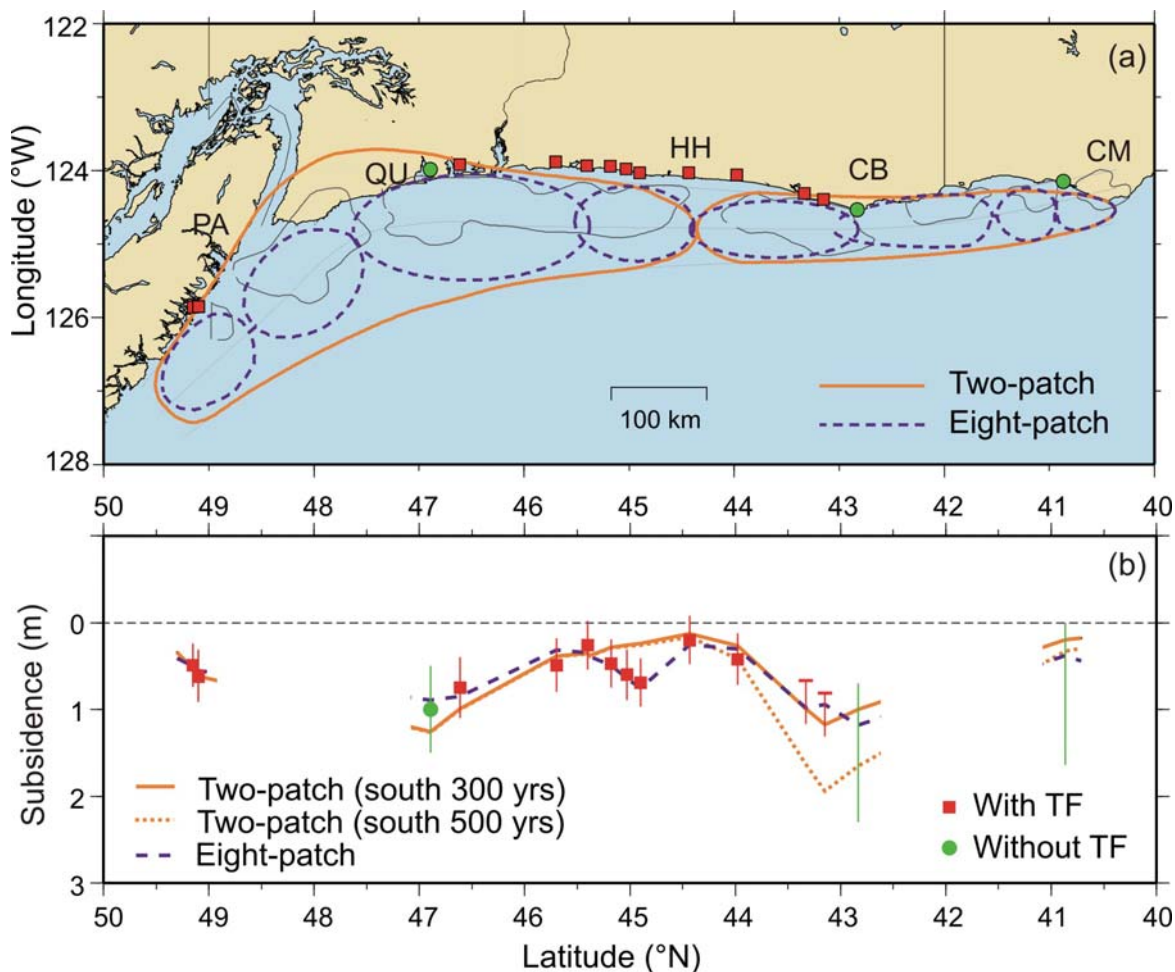


**Figure 5.9.** Test models with different numbers of high-slip patches. (a) Outlines of high-slip patches. Gray lines delineate offshore basins inferred from gravity lows by *Wells et al.* [2003]. PA – Port Alberni, QU – Quinault, HH – Heceta Head, CB – Cape Blanco, CM – Cape Mendocino. (b) Model subsidence at the observation sites. For the two-patch model (orange), slip of the north patch is 450 yrs, and slip of the south patch is 300 or 500 yrs.

The eight-patch model fits the paleoseismic observations in southwestern Washington better than the preferred model. With the preferred model, there is difficulty fitting the

paleoseismic subsidence estimates in both southern Washington and on Vancouver Island. For example, a narrower slip patch off northern Washington would lead to greater subsidence on the coast of Vancouver Island. The eight-patch model does a better job in this regard. Although the model prediction is improved by introducing segmentation boundaries in the northern Cascadia, I preferred not to introduce boundaries in areas where there are data gaps. However, there are arguments that some boundaries in this region may be needed. For example, by studying earthquake-induced debris flows in an inlet near Victoria on the east side of Vancouver Island, *Blais-Stevens et al.* [2011] proposed that the average recurrence of strong earthquake shaking interval is about 220 years. This is higher than subsidence events defining great earthquakes in southern Washington [*Atwater et al.*, 1995], and it is unlikely that the inlet debris-flows have a one-to-one correlation with megathrust earthquakes as strong local earthquakes are a likely cause of some debris flow events. Based on the offshore turbidite records, *Atwater and Griggs* [2012] pointed out that the earthquake frequency offshore southern British Columbia and northern Washington may be higher than that further south. Future paleoseismic data from southern Vancouver Island, northern Washington and northern California will help distinguish between the preferred model and more complex models such as this eight-patch model.

## **5.6. Discussion**

### **5.6.1. Model Predictions in the Data Gap**

In areas where paleoseismic observations are not available, such as northern and southern Cascadia, the models are not constrained. To further emphasize the importance

of making paleoseismic observations in these critical areas, I show in Figure 5.10 predictions of surface deformation continuously along the coastline by several models, instead of predictions only at the sites of paleoseismic estimates. The four models shown can all fit the paleoseismic observations. Although predictions by these models are more or less mutually consistent in the central and southern Cascadia, none of the models are constrained by good data in this area. The predictions by different models in northern Cascadia show large differences (Figure 5.10). For example, along the coast of northern Washington ( $47^{\circ}\text{N} \sim 48.5^{\circ}\text{N}$ ), the subsidence predicted by the preferred and eight-patch models is roughly  $\sim 1$  m. However, subsidence predicted by the Narrow+200 model is up to  $\sim 3$  m. The Wide-200 Model predicts uplift. .

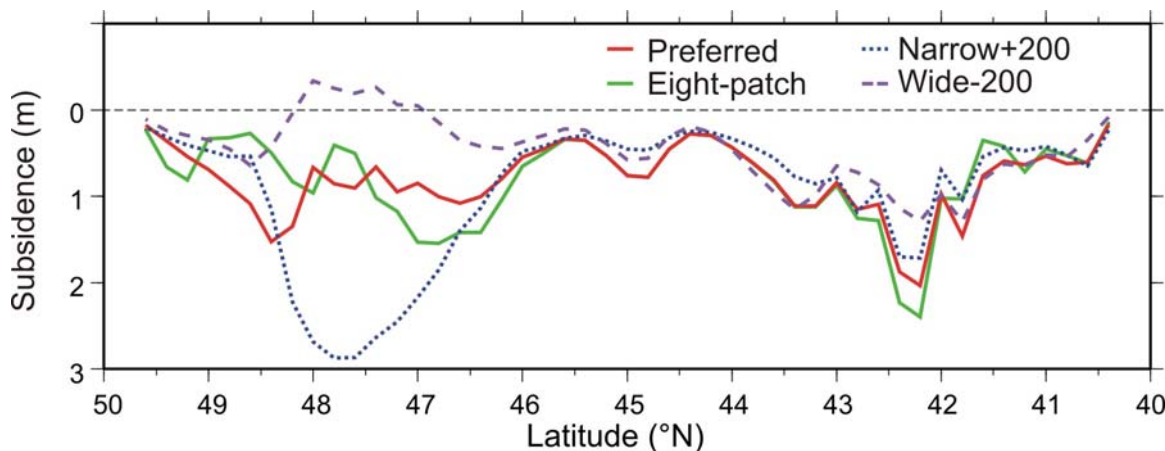


**Figure 5.10.** Model-predicted surface deformation by the preferred, Eight-patch, Narrow+200, and Wide-200 models continuously along the coast of Cascadia margin. Most of the sites of paleoseismic observations shown in other figures are in inlets and estuaries and thus are landward of the smoothed coast line used here.

### 5.6.2. Slip Deficit and Earthquake Recurrence Interval

Similar to the heterogeneous rupture seen in other subduction zone earthquakes, the preferred model features strong along-strike variations represented by a series of slip patches with different slip deficits. The equivalent time period required to accumulate the slip in the preferred model does not represent earthquake recurrence interval. There are some inconsistencies between the preferred model and paleoseismic studies. For examples, paleoseismic data indicated short preceding interval of strain accumulation time (~200 years) in northern Cascadia [*Leonard et al.*, 2010], which is smaller than that in the preferred model (450 years). Based on offshore turbidite deposits, *Goldfinger et al.* [2008] proposed that the earthquake recurrence times show a decreasing pattern southward, from about 520 years in northern Cascadia, to about 220 years or less in southern Cascadia. This earthquake recurrence interval is much smaller than that in the preferred model (550 years and 450 years, see Table 5.1). That is, the slip deficit accumulated during averaged interseismic period may not be responsible for the relatively large slip during the 1700 Cascadia earthquake.

The inconsistency between the magnitude of coseismic slip and the slip magnitude deduced from strain accumulation could be explained by postseismic deformation and long-term energy cycles. Coseismic rupture in one earthquake can be larger than that predicted by strain accumulation since its predecessor. Based on the 10,000-year Cascadia turbidite record, *Goldfinger et al.* [2010] pointed out that the inter-event time may not directly correlate to the magnitude of predicted coseismic slip, because of the long-term energy cycling involved in many earthquake cycles. They suggested that some events may recover less accumulated energy, while other events may release more. The latter may have borrowed unspent energy from previous events or energy from future

events.

## Chapter 6. Conclusions and Recommendations for Future Research

### 6.1. Conclusions

Like all instrumentally recorded megathrust earthquakes of the past half century worldwide, great Cascadia earthquakes must have exhibited heterogeneous coseismic slip. Past Cascadia earthquake models assumed uniform along-strike rupture because the large scatter and errors of paleoseismic observations did not allow resolution for higher order variations. In this work, I use recently obtained higher-quality estimates of coseismic coastal subsidence based on the analyses of intertidal microfossils, in most cases by applying the transfer function method with foraminiferal microfossil assemblages.

A rupture scenario is developed for the M~9 earthquake of AD 1700 consisting of high-slip patches separated by low-slip areas. The surface deformation is modeled using a 3-D elastic half-space dislocation model. The locations of the high- and low-slip areas are constrained by estimates of coseismic subsidence based on microfossil observations. The preferred model (Figure 5.3) consists of four high-slip patches. There are two large areas in northern and southern Cascadia where TF-assisted microfossil paleoseismic data are either very inadequate or not present at all. Therefore, the slip values of these parts of these models are not or very poorly constrained. For lack of constraints and for simplicity, large slip patches are assigned to these areas in the preferred model, but the possibility of more heterogeneous rupture in these areas is by no means excluded. The model serves as a working hypothesis for the AD 1700 rupture testable by future paleoseismic observations.

The location of some of our low-slip areas appears to coincide with previously speculated segmentation boundaries or geological features. For example, there is a reported subducting seamount roughly at the latitude of Alsea Bay ( $\sim 44.5^{\circ}\text{N}$ ) [Trehu *et al.*, 2008]. The location of the high-slip patches is in some agreement with the location of forearc basins offshore inferred by Wells *et al.* [2003] from gravity anomalies. If the model can be validated by more paleoseismic observations, it raises important scientific questions such as whether the low-slip areas are controlled by geological processes and the implications of that for seismic hazard mapping.

Although the coastal subsidence data used here help define along-strike slip variations, they cannot constrain rupture width in the dip direction. Because of the lack of data coverage in the dip direction, there is a trade-off between slip magnitude and the position of the downdip rupture limit. A wider rupture with smaller slip and a narrower rupture with greater slip can both fit the coastal data. Also, the coastal data contain no information on the rupture behaviour of the updip half of the rupture zone. Although in the preferred model of this work the slip decreases to zero at the deformation front, it does not exclude the possibility of very large slip in this area.

## **6.2. Recommendations for Future Research**

The results of this modeling study not only demonstrate the value of high quality microfossil data that can resolve along-strike variations in coseismic land-level changes, but also shows the importance of acquiring such data at high spatial density and along the full range of the margin.

Due to the paucity of data in northern and southern Cascadia, slip distribution of the 1700 great earthquake in these areas is poorly constrained. In northern Cascadia, especially northern Washington, surface deformation depends very sensitively on small changes in fault slip (Figure 5.10). As discussed in Section 5.6.1, downdip rupture extent in northern Washington is not constrained except for assumptions based on thermal arguments; predictions by various models show large differences. Although the distribution of some high slip areas coincides with offshore basins (Figure 5.9), the distribution of high slip areas in northern and southern Cascadia is unknown due to the paucity of paleoseismic observations. In these regions, stratigraphic studies such as offshore turbidite deposits and slumps near the deformation front can help to reconstruct ancient earthquakes. The variation of earthquake frequencies along the Cascadia margin based on paleoseismic studies, especially those using offshore turbidite records, may help distinguish between segments of different recurrence behaviour. Future microfossil-based estimates of coseismic subsidence between southwestern Vancouver Island and northern Washington will be the most valuable in improving future rupture models.

In addition to spatial coverage of paleoseismic observations, high-quality data are needed especially in southern Cascadia. Because of the more than 1 m uncertainties in the estimates in Sixes River and Humboldt Bay, rupture in these regions is not well constrained. Rupture in northern and southern Cascadia might be small because of the possibly high earthquake frequency in these regions that might be inferred from debris flows in an inlet on the east coast of Vancouver Island [Blais-Stevens *et al.*, 2011] and turbidite deposits offshore southern Cascadia [Goldfinger *et al.*, 2008]. Therefore, microfossil-based estimates of coseismic subsidence, in particular the use of TF, are

critical to improving model resolution.

This study uses an elastic model to simulate coseismic subsidence because rupture behavior of the megathrust is known to be elastic. However, due to the uncertainties in paleo-elevation reconstruction as discussed in Section 2.4.2, coseismic elevation change inferred from paleoseismic observations may be contaminated by postseismic deformation. Future viscoelastic models will help to assess the effect of postseismic deformation. Surface deformation due to afterslip and postseismic mantle relaxation could be used to refine the paleoseismic estimates.

In addition to paleoseismic observations and models that constrain coseismic deformation, the interseismic behavior of the Cascadia megathrust also requires more detailed investigation. High and low slip areas during an earthquake should behave differently during the interseismic period, so that the overall slip budget is in balance. If the high and low slip areas during the 1700 Cascadia earthquake are due to permanent features, the high slip areas may be locked during the interseismic period, and the low slip areas may continue to creep. Identifying locking or creeping states along the Cascadia margin is critical for understanding coseismic rupture in the past and in the future. However, it is presently unclear to what degree the interseismically locked and creeping segments can be resolved. Based on the inversion of GPS observations to solve simultaneously for the degree of megathrust locking and the rates of motion of a number of upper-plate crustal blocks, *McCaffrey et al.* [2007] suggest that large portions of the megathrust in northern and southern Cascadia are presently creeping, but the suggested creeping segments are not correlated with the pattern of 1700 coseismic slip proposed in the present study. Current GPS observations can also be explained by assuming a fully

locked megathrust [Wang *et al.*, 2003]. Our view of the locking state of the Cascadia subduction fault is limited by (1) the poor resolving power of land-based GPS networks that are located very far from the megathrust seismogenic zone, and (2) large signals of secular geological deformation in the upper plate that may mask some of the signals of interseismic deformation. Therefore, observations near the deformation front using seafloor geodesy are critical for fully understanding the interseismic behaviour of the megathrust.

Creeping of the megathrust is expected to be accompanied by small thrust earthquakes unless creep is fully aseismic. The Cascadia megathrust is well known to be seismically very quiet at present. Except for a few events ( $M > 4.7$ ) reported off Oregon [Tréhu *et al.*, 2011], there are essentially no reported megathrust earthquakes of any size. As discussed in Section 1.2, this has been considered as supporting evidence for the complete locking of the megathrust fault. However, the apparent absence of megathrust seismicity may be due partly to the fact that the seismic stations are land based and too far from the source to detect very small events. More near-source observations will improve our understanding of seismicity in Cascadia. For example, NEPTUNE Canada, a fibre-optic cable observatory that covers much of the northern part of the Juan de Fuca plate, includes seismometers and subsea borehole observatories. The borehole observatories can detect pore fluid pressure changes associated with seismic and aseismic strain change due to tectonic deformation [Davis and Petronotis, 2010]. In addition, ocean bottom seismometers (OBS) installed under the ongoing project of Seafloor Earthquake Array–Japan–Canada Cascadia Experiment (SeaJade) [Scherwarth *et al.*, 2011] will help to identify small earthquake signals, and potentially even episodic tremor

and slip (ETS) and very low frequency (VLF) earthquakes induced by creeping of the plate interface, especially near the deformation front.

Seismic analyses can help to characterize along-strike segmentation of the Cascadia margin and geometrical irregularities such as subducting seamounts that act as barrier structures during great earthquakes [*Wang and Bilek, 2011*]. Structural segmentation inferred from seismic surveys will improve the understanding of seismic behavior and should be compared with paleoseismic observations such as those presented in this thesis. As more detailed observations and accordingly refined theoretical models become available, we will have a better understanding of the Cascadia subduction zone earthquake processes. Such understanding is critical to the development of realistic earthquake and tsunami hazard models.

## Bibliography

- Ammon, C. J., C. Ji, H. K. Thio, D. Robinson, S. Ni, V. Hjorleifsdottir, H. Kanamori, T. Lay, S. Das, G. Helmberger, G. Ichinose, J. Polet, D. Wald (2005), Rupture process of the 2004 Sumatra–Andaman earthquake, *Science*, 308, 1133–1139, doi: 0.1126/science.1112260.
- Atwater, B. F. (1987), Evidence for great Holocene earthquakes along the outer coast of Washington state, *Science*, 236, 942–944.
- Atwater, B. F. (1992), Geologic evidence for earthquakes during the past 2000 years along the Copalis River, southern coastal Washington, *Journal of Geophysical Research*, 97, 1901–1919, doi: 10.1029/91JB02346.
- Atwater, B. F., and G. B. Griggs (2012), Deep-sea turbidites as guides to Holocene earthquake history at the Cascadia Subduction Zone—Alternative views for a seismic-hazard workshop, *U.S. Geological Survey Open-File Report*, 2012–1043, 58 p., available at <http://pubs.usgs.gov/of/2012/1043/>.
- Atwater, B. F., and E. Hemphill-Haley (1997), Recurrence intervals for great earthquakes of the past 3500 years at northeastern Willapa Bay, Washington, *U.S. Geological Survey Professional Paper*, 1576, 108.
- Atwater, B. F., and D. Yamaguchi (1991), Sudden, probably coseismic submergence of Holocene trees and grass in coastal Washington state, *Geology*, 19(7), 706–709.
- Atwater, B. F., A. R. Nelson, J. J. Clague, G. A. Carver, P. T. Bobrowsky, J. Bourgeois, M. E. Darienzo, W. C. Grant, E. Hemphill-Haley, H. M. Kelsey, C. G. Jacoby, S. P. Nishenko, S. Palmer, C. D. Peterson, M. A. Reinhart, and D. K. Yamaguchi (1995), Summary of coastal geologic evidence for past great earthquakes at the Cascadia subduction zone, *Earthquake Spectra*, 11, 1–18.
- Atwater, B. F., M. P. Tuttle, E. S. Schweig, C. M. Rubin, D. K. Yamaguchi, and E. Hemphill-Haley (2004), Earthquake recurrence inferred from paleoseismology, in *The Quaternary Period in the United States*, Elsevier Science, edited by A. R. Gillespie et al., pp. 331–350, New York,.
- Atwater, B. F., S. Musumi-Rokkaku, K. Satake, Y. Tsuji, K. Ueda, and D. K. Yamaguchi (2005), The orphan tsunami of 1700—Japanese clues to a parent earthquake in North America, *U.S. Geological Survey Professional Paper*, 1707.
- Benson, B. E., K. A. Grimm, and J. J. Clague (1997), Tsunami deposits beneath tidal marshes on northwestern Vancouver Island, British Columbia, *Quaternary Research*, 48, 192–204.

- Bilek, S. L., and T. Lay (1999), Rigidity variations with depth along interplate megathrust faults in subduction zones, *Nature*, 400, 443-446.
- Birks, H. J. B. (1995), Quantitative paleoenvironmental reconstructions, in *Statistical Modeling of Quaternary Science Data*, Technical Guide no.5, edited by D. Maddy, J. S., Brew, pp.161–236, Quaternary Research Association, Cambridge.
- Blais-Stevens, A., G. C. Rogers, and J. J. Clague (2011), A revised earthquake chronology for the last 4,000 years inferred from varve-bounded debris-flow deposits beneath an inlet near Victoria, British Columbia, *Bulletin of the Seismological Society of America*, 101, 1–12, doi:10.1785/0120090360.
- Chlieh, M., J.-P. Avouac, V. Hjorleifsdottir, T.-R. A. Song, C. Ji, K. Sieh, A. Sladen, H. Hebert, D. H. Natawidjaja, and J. Galetzka (2007), Coseismic slip and afterslip of the great (M<sub>w</sub>9.15) Sumatra-Andaman earthquake of 2004, *Bulletin of the Seismological Society of America*, 97, S152–S173.
- Clague, J. J. (1995), Early historical and ethnographical accounts of large earthquakes and tsunamis on western Vancouver Island, British Columbia, *Current research, 1995-A*, 47–50, Geological Survey of Canada., Ottawa, Ontario.
- Clague, J. J. (1997), Evidence for large earthquakes at the Cascadia subduction zone, *Reviews of Geophysics*, 35, 439–460.
- Clague, J.J., and P. T. Bobrowsky (1994). Evidence for a large earthquake and tsunami 100-400 years ago on western Vancouver Island, British Columbia. *Quaternary Research*, 41, 176-184.
- Clague, J. J., P. T. Bobrowsky, I. Hutchinson, and R. W. Mathewes (1998), Geological evidence for past large earthquakes in southwest British Columbia, *Current Research 1998-A*, 217–224, Geological Survey of Canada., Ottawa, Ontario.
- Clague, J. J., I. Hutchinson, R. W. Mathewes, and R. T. Patterson (1999), Evidence for late Holocene tsunamis at Catala Lake, British Columbia, *Journal of Coastal Research*, 15(1), 45–60.
- Clague, J. J., P. T. Bobrowsky, and I. Hutchinson (2000), A review of geological records of large tsunamis at Vancouver Island, British Columbia, and implications for hazard, *Quaternary Science Reviews*, 19, 849-863.
- Cohen, S. C., and J. T. Freymueller (2001), Crustal uplift in the south central Alaska subduction zone: New analysis and interpretation of tide gauge observations, *Journal of Geophysical Research*, 106, 653 – 668.
- Coulter, H. W., and R. R. Migliaccio (1966), Effects of the earthquake of March 27, 1964, at Valdez, Alaska, *U.S. Geological Survey Professional Paper*, 542-C, C1-C36.

- Culver, S. J., B. P. Horton, (2005), Infaunal marsh foraminifera from the Outer Banks, North Carolina, *Journal of Foraminiferal Research*, 35, 148–170.
- Davis, E. E., and K. E. Petronotis [2010], Cascadia subduction zone ACORK observatory, *integrated Ocean Drilling Program Scientific Prospectus*, 328, 73–84, doi:10.2204/iodp.sp.328.2010.
- Darrienzo, M. E., and C. D. Peterson (1990), Episodic tectonic subsidence of late Holocene salt marshes, northern Oregon, central Cascadia margin, *Tectonics*, 9, 1–22, doi: 10.1029/TC009i001p00001.
- Darrienzo, M. E., and C. D. Peterson (1995), Magnitude and frequency of subduction-zone earthquakes along the northern Oregon coast in the past 3,000 years, *Oregon Geology*, 57, 3–12.
- Darrienzo, M. E., C. D. Peterson, and C. Clough (1994), Stratigraphic evidence for great subduction-zone earthquakes at four estuaries in northern Oregon, U.S.A., *Journal of Coastal Research*, 10(4), 850–876.
- Delouis, B., J.-M. Nocquet, and M. Vallée (2010), Slip distribution of the February 27, 2010 Mw = 8.8 Maule earthquake, central Chile, from static and high-rate GPS, InSAR, and broadband teleseismic data, *Geophysical Research Letters*, 37, L17305, doi:10.1029/2010GL043899
- Dragert, J., and R. D. Hyndman (1995), Continuous GPS monitoring of elastic strain in the northern Cascadia subduction zone, *Geophysical Research Letters*, 22, 755–758.
- Dragert, H., R. D. Hyndman, G. C. Rogers, and K. Wang (1994), Current deformation and the width of the seismogenic zone of the northern Cascadia subduction thrust, *Journal of Geophysical Research*, 99, 653–668, doi: 10.1029/93JB02516.
- Edwards, R. J., A. J. Wright, O. van de Plassche (2004), Surface distribution of salt-marsh foraminifera from Connecticut, USA: Modern analogues for high resolution sea-level studies, *Marine Micropaleontology*, 51, 1–21.
- Eilers, H. (1975), Plants, plant communities, net production and tide levels: The ecological biogeography of the Nehalem salt marshes, Ph.D. Thesis, Oregon State University, Tillamook County, Oregon, 368pp.
- Fariás, M., G. Vargas, A. Tassara, S. Carretier, S. Baize, D. Melnick, K. Bataille (2010), Land-level changes produced by the Mw 8.8 2010 Chilean earthquake, *Science*, 329, 916, doi: 10.1126/science.1192094.
- Flück, P., R. D. Hyndman, and K. Wang (1997), Three-dimensional dislocation model for great earthquakes of the Cascadia subduction zone, *Journal of Geophysical Research*, 102(20), 539–550.

- Freund, L. B., and D. M. Barnett (1976), A two-dimensional analysis of surface deformation due to dip-slip faulting, *Bulletin of the Seismological Society of America*, 66, 667–675.
- Fujii, Y., K. Satake, S. Sakai, M. Shinohara, and T. Kanazawa (2011), Tsunami source of the 2011 off the Pacific coast of Tohoku Earthquake, *Earth Planets Space*, 63, 815–820.
- Fujiwara, T., S. Kodaira, T. No, Y. Kaiho, N. Takahashi, and Y. Kaneda (2011), Tohoku-Oki earthquake: Displacement reaching the trench axis, *Science*, 334(6060), 1240, doi: 10.1126/science.1211554
- Goldfinger, C., C. H. Nelson, and J. E. Johnson (2003), Holocene earthquake records from the Cascadia subduction zone and northern San Andreas fault based on precise dating of offshore turbidities, *Annual Review of Earth and Planetary Sciences*, 31, 555–577, doi: 10.1146/annurev.earth.31.100901.141246.
- Goldfinger, C., K. Grijalva, R. Bürgmann, A. E. Morey, J. E. Johnson, H. Nelson, J. Gutiérrez-Pastor, A. Ericsson, E. Karabanov, J. D. Chaytor, J. Patton, and E. Gràcia (2008), Late Holocene rupture of the northern San Andreas fault and possible stress linkage to the Cascadia subduction zone, *Bulletin of the Seismological Society of America*, 8(2), 861–889, doi: 10.1785/0120060411.
- Goldfinger, C., C. H. Nelson, J. E. Johnson, A. E. Morey, J. Gutiérrez-Pastor, E. Karabanov, A. T. Eriksson, E. Gràcia, G. Dunhill, J. Patton, R. Enkin, A. Dallimore, T. Vallier, and the shipboard scientific parties (2009), Turbidite event history: methods and implications for Holocene paleoseismicity of the Cascadia subduction zone, *U.S. Geological Survey Professional Paper*, 1661-F.
- Goldfinger, C., R. Witter, G. R. Priest, K. Wang, and Y. Zhang (2010), Cascadia supercycles—Energy management of the long Cascadia earthquake series, Seismological Society of America 2010 Annual Meeting, *Seismological Research Letters*, 81, 290.
- Goldfinger, C., C. H. Nelson, A. Morey, J. E. Johnson, J. Gutierrez-Pastor, A.T. Eriksson, E. Karabanov, J. Patton, E. Gracia, R. Enkin, A. Dallimore, G. Dunhill, and T. Vallier (2012), Turbidite event history: Methods and implications for Holocene paleoseismicity of the Cascadia Subduction Zone, *U.S. Geological Survey Professional Paper*, 1661-F.
- Goldstein, S. T., and G. T. Watkins, (1999), Taphonomy of salt marsh foraminifera: An example from coastal Georgia, *Palaeogeography, Palaeoclimatology, Palaeoecology*, 149, 103–114.
- Guilbault, J. P., J. J. Clague, and M. Lapointe (1995), Amount of subsidence during a late Holocene earthquake—Evidence from fossil tidal marsh foraminifera at Vancouver Island, west coast of Canada, *Palaeogeography, Palaeoclimatology, Palaeoecology*, 118, 49–71, doi: 10.1016/0031-0182(94)00135-U.

- Guilbault, J. P., J. J. Clague, and M. Lapointe (1996), Foraminifera evidence for the amount of coseismic subsidence during a late Holocene earthquake on Vancouver Island, west coast of Canada, *Quaternary Science Reviews*, *15*, 913–937, doi: 10.1016/S0277-3791(96)00058-3.
- Hanks, T. C. And H. Kanamori (1979), A moment magnitude scale. *Journal of Geophysical Research*, *84*, 2348–2350.
- Hawkes, A. D., B. P. Horton, A. R. Nelson, D. F. Hill (2010), The application of intertidal foraminifera to reconstruct coastal subsidence during the giant Cascadia earthquake of AD 1700 in Oregon, *Quaternary International*, *221*, 116–140.
- Hawkes, A. D., B. P. Horton, A. R. Nelson, C. H. Vane, and Y. Sawai (2011), Coastal subsidence in Oregon, USA, during the giant Cascadia earthquake of AD 1700, *Quaternary Science Reviews*, *30*, 364–376, doi:10.1016/j.quascirev.2010.11.017.
- Hemphill-Haley, E. (1995), Diatom evidence for earthquake induced subsidence and tsunami 300 yr ago in southern coastal Washington, *Geological Society of America Bulletin*, *107*, 367–378, doi: 10.1130/0016-7606(1995)107<0367:DEFEIS>2.3.CO;2.
- Hirose, T., and M. Bystricky (2007), Extreme dynamic weakening of faults during dehydration by coseismic shear heating, *Geophysical Research Letters*, *34*, L14311, doi:10.1029/2007GL030049.
- Horton, B. P. (1999), The contemporary distribution of intertidal foraminifera of Cowpen Marsh, Tees Estuary, UK: Implications for studies of Holocene sea-level changes, *Palaeogeography, Palaeoclimatology, Palaeoecology*, *149*, 127–149.
- Horton, B. P., and B. P. Edwards (2006), Quantifying Holocene sea-level change using intertidal foraminifera: Lessons from the British Isles, *Cushman Foundation for Foraminiferal Research, Special Publication 40*, 97 pp.
- Horton, B. P., S. E. Engelhart, A. C. Kemp, Y. Sawai (2012), Microfossils in tidal settings as indicators of sea-level change, paleoearthquakes, tsunamis, and tropical cyclones, in *Treatise on Geomorphology*, vol. 14, edited by Shroder, J., A. D. Switzer, D. Kennedy, Academic, San Diego, California.
- Hu, Y., and K. Wang (2008), Coseismic strengthening of the shallow portion of the subduction fault and its effects on wedge taper, *Journal of Geophysical Research*, *113*, B12411, doi:10.1029/2008JB005724.
- Hughes, J. F., R. W. Mathewes, and J. J. Clague (2002), Use of pollen and vascular plants to estimate coseismic subsidence at a tidal marsh near Tofino, British Columbia, *Palaeogeography, Palaeoclimatology, Palaeoecology*, *185*, 145–161, doi: 10.1016/S0031-0182(02)00283-3.
- Hyndman, R. D. (1995), Giant earthquakes of the Pacific Northwest, *Scientific American*, *273*, 50–57.

- Hyndman, R. D., and K. Wang (1993), Thermal constraints on the zone of major thrust earthquake failure: The Cascadia subduction zone, *Journal of Geophysical Research*, 98, 2039–2060, doi: 10.1029/92JB02279.
- Hyndman, R. D., and K. Wang (1995), The rupture zone of Cascadia great earthquakes from current deformation and thermal constraints on the zone of potential great earthquakes on the Cascadia subduction thrust, *Journal of Geophysical Research*, 100(22), 133–154.
- Hyndman, R. D., L. J. Leonard, C. A. Currie (2005), Test of models for the Cascadia great earthquake rupture area using coastal subsidence estimates for the 1700 earthquake, *Final Report, US Geological Survey NEHRP External Grant Award*, 04HQGR0088, 11pp.
- Ide, S., A. Baltay, and G. Beroza (2011), Shallow dynamic overshoot and energetic deep rupture in the 2011 Mw 9.0 Tohoku-Oki earthquake, *Science*, 332(6036)1426-1429, doi:10.1126/science.1207020.
- Jacoby, G. C., D. E. Bunker, and B. E. Benson (1997), Tree-ring evidence for an A.D. 1700 Cascadia earthquake in Washington and northern Oregon, *Geology*, 25, 999–1002.
- Jonasson, K. E., R. T. Patterson (1992), Preservation potential of salt marsh foraminifera from the Fraser River delta, British Columbia, *Micropaleontology*, 38, 289–301.
- Kachadorian, R. (1965), Effects of the earthquake of March 27, 1964, at Whittier, Alaska, *U.S. Geological Survey Professional Paper*, 542-B, B1-B21.
- Kelsey, H. M., R. C. Witter, and E. Hemphill-Haley (1998), Response of a small Oregon estuary to coseismic subsidence and postseismic uplift in the past 300 years, *Geology*, 26(3), 231–234, doi: 10.1130/0091-7613(1998)026<0231:ROASOE>2.3.CO;2.
- Kelsey, H. M., R. C. Witter, E. Hemphill-Haley (2002), Plate-boundary earthquakes and tsunamis of the past 5500 years, Sixes River estuary, southern Oregon, *Geological Society of America Bulletin*, 114, 298–314.
- Kelsey, H. M., A. R. Nelson, E. Hemphill-Haley, R. Witter (2005), Tsunami history of an Oregon coastal lake reveals a 4600 yr record of great earthquakes on the Cascadia subduction zone, *Geological Society of America Bulletin*, 117, 1009–1032.
- Leonard, L. J., R. D. Hyndman, and S. Mazzotti (2004), Coseismic subsidence in the 1700 great Cascadia earthquake: Coastal estimates versus elastic dislocation models, *Geological Society of America Bulletin*, 116, 655–670, doi: 10.1130/B25369.1.
- Leonard, L. J., C. A. Currie, S. Mazzotti, and R. D. Hyndman (2010), Rupture area and displacement of past Cascadia great earthquakes from coastal coseismic subsidence, *Geological Society of America Bulletin*, 122, 2079–2096, doi:10.1130/B30108.1.

- Lisowski, M., W. H. Prescott, H. Dragert, and S. R. Holdahl (1989), Results from 1986 and 1987 GPS survey across the Strait of Juan de Fuca, Washington and British Columbia, *Seismological Research Letters*, 60, 1.
- Lorito, S., F. Romano, S. Atzori, X. Tong, A. Avallone, J. McCloskey, M. Cocco, E. Boschi, and A. Piatanesi (2011), Limited overlap between the seismic gap and coseismic slip of the great 2010 Chile earthquake, *Nature Geoscience*, 4(3), 173–177, doi:10.1038/ngeo1073.
- McCaffrey, R., A. I. Qamar, R. W. King, R. Wells, G. Khazaradze, C. A. Williams, C. W. Stevens, J. J. Vollick, and P. C. Zwick (2007), Fault locking, block rotation and crustal deformation in the Pacific Northwest, *Geophysical Journal International*, 169, 1315–1340, doi: 10.1111/j.1365-246X.2007.03371.
- McCrorey, P. A., J. L. Blair, S. H. Oppenheimer, S. R. Walter (2004), Depth to the Juan de Fuca slab beneath the Cascadia subduction margin—a 3-D model for sorting earthquakes, *US Geological Survey Data Series, DS-91*.
- Murray, J. W. (2000), The enigma of the continued use of total assemblages in ecological studies of benthic foraminifera, *Journal of Foraminiferal Research*, 30, 244–245.
- Nelson, A.R., and K. Kashima (1993), Diatom zonation in southern Oregon tidal marshes relative to vascular plants, foraminifera, and sea level, *Journal of Coastal Research*, 9, 673–697.
- Nelson, A. R., B. F. Atwater, P. T. Bobrowsky, L. A. Bradley, J. J. Clague, G. A. Carver, M. E. Darienzo, W. C. Grant, H. W. Kreuger, R. Sparks, T. W. Stafford, and M. Stuiver (1995), Radiocarbon evidence for extensive plateboundary rupture about 300 years ago at the Cascadia subduction zone, *Nature*, 378, 371–374.
- Nelson, A. R., I. Shennan, and A. J. Long (1996a), Identifying coseismic subsidence in tidal-wetland stratigraphic sequences at the Cascadia subduction zone of western North America, *Journal of Geophysical Research*, 101(B3), 6115–6135, doi: 10.1029/95JB01051.
- Nelson, A. R., A. E. Jennings, and K. Kashima (1996b), An earthquake history derived from stratigraphic and microfossil evidence of relative sea-level change at Coos Bay, southern coastal Oregon, *Geological Society of America Bulletin*, 108, 141–154.
- Nelson, A. R., A. C. Asquith, and W. C. Grant (2004), Great earthquakes and tsunamis of the past 2000 years at the Salmon River estuary, central Oregon coast, USA, *Bulletin of Seismological Society of America*, 94, 1276–1292.
- Nelson, A. R., H. M. Kelsey, and R. C. Witter (2006), Great earthquakes of variable magnitude at the Cascadia subduction zone, *Quaternary Research*, 65, 354–365, doi: 10.1016/j.yqres.2006.02.009.

- Nelson, A. R., Y. Sawai, A. E. Jennings, L.-A. Bradley, L. Gerson, B. L. Sherrod, J. Sabeau, and B. P. Horton (2008), Great-earthquake paleogeodesy and tsunamis of the past 2000 years at Alsea Bay, central Oregon coast, *Quaternary Science Reviews*, 27, 747–768, doi: 10.1016/j.quascirev.2008.01.001.
- Ng, M. K.-F., P. H. LeBlond, and T. S. Murty (1991), Simulation of tsunamis from great earthquakes on the Cascadia subduction zone, *Science*, 250, 1248-1251.
- Okada, Y. (1985), Surface deformation due to shear and tensile faults in a halfspace, *Bulletin of the Seismological Society of America*, 75, 1135–1154.
- Okada, Y. (1992), Internal deformation due to shear and tensile faults in a half space, *Bulletin of the Seismological Society of America*, 82, 1018–1040.
- Oleskevich, D. A., R. D. Hyndman, and K. Wang (1999), The updip and downdip limits to great subduction earthquakes: Thermal and structural models of Cascadia, south Alaska, SW Japan, and Chile, *Journal of Geophysical Research*, 104, 14,965–14,991.
- Ovenshine, A. T., D. E. Lawson, and S. R. Bartsch-Winkler (1976), The Placer River Silt—An intertidal deposit caused by the 1964 Alaska earthquake, *U.S. Geological Survey Journal of Research*, 4, 151–162.
- Peterson, C. D., and M. E. Darienzo (1991), Discrimination of climatic, oceanic and tectonic mechanisms of cyclic marsh burial from Alsea Bay, Oregon, USA, *U.S. Geological Survey Open File Report*, 91–441-C, 53 p.
- Peterson, C. D., D. L. Doyle, and E. T. Barnett (2000), Coastal flooding and beach retreat from coseismic subsidence in the central Cascadia margin, USA, *Env. Eng. Geosci.*, 6, 255-269.
- Porritt, R. W., R. M. Allen, D. C. Boyarko, and M. R. Brudzinski (2011), Investigation of Cascadia segmentation with ambient noise tomography, *Earth and Planetary Science Letters*, 309, 67–76, doi:10.1016/j.epsl.2011.06.026.
- Priest, G. R., K. Wang, Y. Zhang, C. Goldfinger, R. Witter, C. D. Peterson, K. Cruikshank, A. M. Baptista, C. Seaton, and P. Turner (2009), Confidence levels for tsunami-inundation limits in northern Oregon inferred from a 10,000-year history of great earthquakes at the Cascadia subduction zone, *Natural Hazards*, 54(1), 19p. doi: 10.1007/s11069-009-9453-5
- Pritchard, C. J. (2004), Late Holocene Relative Sea-Level Changes, Arcata Bay, California: Evaluation of Freshwater Syncline movement using coseismically buried soil Horizons, M.S. thesis, Humboldt State University, Department of Geology, Arcata, California, 56 p.
- Reilinger, R. and J. Adams (1982), Geodetic evidence for land ward tilting of the Oregon and Washington coastal areas, *Geophysical Research Letters*, 9, 401-403.

- Sabeau, J.A.R. (2004), Applications of foraminifera to detecting land level change associated with great earthquakes along the west Coast of North America, M.Sc. thesis, Simon Fraser University, Burnaby, British Columbia, 90 p.
- Satake, K., K. Shimazaki, Y. Tsuji, and K. Ueda (1996), Time and size of a giant earthquake in Cascadia inferred from Japanese tsunami records of January 1700, *Nature*, 379 (6562), 246–249, doi:10.1038/379246a0.
- Satake, K., K. Wang, and B. F. Atwater (2003). Fault slip and seismic moment of the 1700 Cascadia earthquake inferred from Japanese tsunami descriptions, *Journal of Geophysical Research B: Solid Earth Planets*, 108 (2325), doi 10.1019/2003JB002521.
- Savage, J. C., and M. Lisowski (1991), Strain measurements and potential for a great subduction earthquake off Oregon and Washington, *Science*, 252, 101-103.
- Shennan, I., A. J. Long, M. M. Rutherford, F. M. Green, J. B. Innes, J. M. Lloyd, Y. Zong, , and K. J. Walker (1996), Tidal marsh stratigraphy, sea-level change and large earthquakes: I. A 5000 year record in Washington, *Quaternary Science Reviews*, 15, 1023–1059, doi: 10.1016/S0277-3791(96)00007-8.
- Shennan, I., A. J. Long, M. M. Rutherford, J. B. Innes, F. M. Green, and K. J. Walker (1998), Tidal marsh stratigraphy, sea-level change and large earthquakes: II. Submergence events during the last 3500 years at Netarts Bay, Oregon, *Quaternary Science Reviews*, 17, 365–393, doi: 10.1016/S0277-3791(97)00055-3.
- Subarya, C., M. Chlieh, L. Prawirodirdjo, J.-P. Avouac, Y. Bock, K. Sieh, A. J. Meltzner, D. H. Natawidjaja, and R. McCaffrey (2006), Plate-boundary deformation associated with the great Sumatra-Andaman earthquake, *Nature*, 440, 46–51, doi: 10.1038/nature04522.
- Tréhu, A. M., J. Braunmiller, and J. L. Nabelek (2008), Probable low-angle thrust earthquakes on the Juan de Fuca–North America plate boundary, *Geology*, 36, 127–130, doi:10.1130/G24145A.1.
- Tréhu, A. M., R. J. Blakely, M. C. Williams (2011), Subducted seamounts and recent earthquakes beneath the central Cascadia forearc, *Geology*, 40, 103-106, doi:10.1130/G32460.1.
- Vigny, C., A. Socquet, S. Peyra, J. C. Ruegg, M. Metois, R. Madariaga, S. Morvan, M. Lancieri, R. Lacassin, J. Campos, D. Carrizo, M. Bejarpizarro, S. Barrientos, R. Armijo, C. Aranda, M. C. Valderas-Bermejo, I. Ortega, F. Bondoux, S. Baize, H. Lyon-Caen, A. Pavez, J. P. Vilotte, M. Bevis, B. Brooks, R. Smalley, H. Parra, J. C. Baez, M. Blanco, S. Climbaro, and E. Kendrick (2011), The 2010 Mw 8.8 Maule megathrust earthquake of central Chile, monitored by GPS, *Science*, 332, 1417–1421, doi:10.1126/science.1204132.

- Wang, K. (2007), Elastic and viscoelastic models of crustal deformation in subduction earthquake cycles, in *The Seismogenic Zone of Subduction Thrust Faults*, edited by T. H. Dixon and J. C. Moore, pp. 540–575, Columbia Univ. Press, New York.
- Wang, K., and S. L. Bilek (2011), Do subducting seamounts generate or stop large earthquakes? *Geology*, 39 (9), 819–822, doi:10.1130/G31856.1.
- Wang, K., and J. He (2008), Effects of frictional behaviour and geometry of subduction fault on coseismic seafloor deformation, *Bulletin of the Seismological Society of America*, 98(2), 571–579, doi: 10.1785/ 0120070097.
- Wang, K., J. He, H. Dragert, and T. S. James (2001), Three-dimensional viscoelastic interseismic deformation model for the Cascadia subduction zone, *Earth Planets Space*, 53, 295–306.
- Wang, K., R. Wells, S. Mazzotti, R. D. Hyndman, and T. Sagiya (2003), A revised dislocation model of interseismic deformation of the Cascadia subduction zone, *Journal of Geophysical Research*, 108(B1), 2026, doi: 10.1029/2001JB001227.
- Wang, K., Y. Hu, and J. He (2012), Deformation cycles of subduction earthquakes in a viscoelastic Earth, *Nature*, 484, 327–332
- Wei, S., Graves, R. Helmberger, D., Avouac, J. –P., and Jiang, J. (2012) Sources of shaking and flooding during the Tohoku-Oki earthquake: A mixture of rupture styles, *Earth and Planetary Science Letters*, 333-334, 91-100, doi: 10.1016/j.epsl.2012.04.006.
- Wells, R. E., and R. W. Simpson (2001), Northward migration of the Cascadia forearc in the northwestern U. S. and implications for subduction deformation, *Earth Planets Space*, 53, 275–283.
- Wells, R. E., C. S. Weaver, and R. J. Blakely (1998), Fore-arc migration in Cascadia and its neotectonic significance, *Geology*, 26, 759–762.
- Wells, R. E., R. J. Blakely, Y. Sugiyama, D. W. Scholl, and P. A. Dinterman (2003), Basin-centered asperities in great subduction zone earthquakes: A link between slip, subsidence, and subduction erosion?, *Journal of Geophysical Research*, 108(B10), 2507, doi:10.1029/2002JB002072.
- Whitmore, P. M. (1993), expected tsunami amplitudes and currents along the North American coast for Cascadia subduction zone earthquakes, *Natural Hazards*, 8, 59–73.
- Wilson, D. S. (1993), Confidence intervals for motion and deformation of Juan de Fuca plate, *Journal of Geophysical Research*, 98, 16053–16071.
- Witter, R. C., H. M. Kelsey, E. Hemphill-Haley (2001), Pacific storms, El Nino and tsunamis: Competing mechanisms for sand deposition in a coastal marsh, Euchre

Creek, Oregon. *Journal of Coastal Research*, 17, 563–583.

Witter, R. C., H. M. Kelsey, and E. Hemphill-Haley (2003), Great Cascadia earthquakes and tsunamis of the past 6700 years, Coquille River estuary, southern coastal Oregon. *Geological Society of America Bulletin*, 115, 1289–1306, doi: 10.1130/B25189.1.

Yamaguchi, D. K., B. F. Atwater, D. E. Bunker, B. E. Benson, and M. S. Reid (1997), Tree-ring dating the 1700 Cascadia earthquake, *Nature*, 389, 922–923, doi: 10.1038/40048.

Yoshida, K., K. Miyakoshi, and K. Irikura (2011), Source process of the 2011 off the Pacific Coast of Tohoku earthquake inferred from waveform inversion with long-period strong-motion records, *Earth Planets Space*, 63, 0–0.